Optical Polarimetry in Be/X-ray binaries: Warped and Precessed Disks During Type-II Outbursts

UNIVERSITY OF CRETE, DEPARTMENT OF PHYSICS

Tzouvanou Anastasia

SUPERVISOR: Dr. Reig Pablo

DISSERTATION

submitted to the

Department of Physics
of University of Crete, Greece

for the degree of

Master of Science

June, 2024

Many thanks to Dr. Blinov Dmitry

Abstract

The mechanisms by which matter from the circumstellar disk of the Be star is transferred to the compact object, which in most cases is a neutron star, to trigger the X-ray outbursts observed in Be/X-ray binaries remain an open question. Current theoretical models suggest that Type-II outbursts occur when the compact object captures an enormous amount of gas from a warped, highly misaligned, and eccentric Be disk. The aim of this work is to test the current theories of warped, highly misaligned, and eccentric Be disk thought optical polarimetry.
We used optical polarimetric observations of three Be/X-ray binaries for ten years, from 2013 until 2023, to explore the characteristics of their disk and compare them with those of classical isolated Be stars without companion.
Our results, after accounting for instrumental polarization and interstellar medium effects, show that two out of the three systems exhibit intrinsic polarization similar to isolated Be stars, with polarization degrees below 2%. An exception to this was the third Be/X-ray binary system - EXO 2030+375 - which exhibits intrinsic polarization up to 10%. This high degree of polarization has been associated with the alignment of ferromagnetic grains from the Be disk with the neutron star's magnetic field.
Significant changes over time were observed both in polarization degree as well as in polarization angle in all three binary systems. This variability indicates the presence of a warped and precessed disk, in agreement with theoretical models. The hypothesis that the disk around the Be star grows freely and gets more and more warped, precessed, and eccentric and eventually transfers mass to the neutron star is in line with our observational work. These findings enhance our understanding of the interaction between neutron stars and Be star decretion disks in Be/X-ray binaries.

Σύνοψη

Οι μηχανισμοί με τους οποίους η ύλη από τον περιστρεφόμενο δίσκο αερίου του άστρου Be μεταφέρεται στο συμπαγές αντικείμενο, που στις περισσότερες περιπτώσεις είναι ένας αστέρας νετρονίων, για να προκαλέσει τις εκρήξεις ακτίνων-Χ που παρατηρούνται σε συστήματα Be/X-ray παραμένουν ανοιχτό ερώτημα. Τα τρέχοντα θεωρητικά μοντέλα προτείνουν ότι οι εκρήξεις Τύπου II συμβαίνουν όταν το συμπαγές αντικείμενο συλλαμβάνει τεράστιες ποσότητες αερίου από έναν παραμορφωμένο, εξαιρετικά ανισότροπο και έκκεντρο δίσκο γύρω από Be αστέρι. Σκοπός αυτής της εργασίας είναι να δοκιμάσει τις τρέχουσες θεωρίες σχετικά με την ύπαρξη ενός παραμορφωμένου, εξαιρετικά ανισότροπου και έκκεντρου δίσκου μέσω οπτικής πολωσιμετρίας.

Χρησιμοποιήσαμε παρατηρήσεις τριών συστημάτων Be/X-ray δέκα χρόνων , από το 2013 έως το 2023, για να εξερευνήσουμε τα χαρακτηριστικά των δίσκων τους και να τα συγκρίνουμε με αυτά των κλασικών μεμονωμένων άστρων Be χωρίς την παρουσία συμπαγούς αντικειμένου.

Τα αποτελέσματά μας, αφού λάβουμε υπόψη την πολωσιμετρία των οργάνων και τις επιδράσεις του διαστρικού μέσου, δείχνουν ότι δύο από τα τρία συστήματα παρουσιάζουν εγγενή πόλωση παρόμοια με τα κλασικά μεμονωμένα άστρα Be, με βαθμούς πόλωσης κάτω από 2%. Εξαίρεση σε αυτό ήταν το τρίτο σύστημα Be/X-ray - EXO 2030+375 - το οποίο παρουσιάζει εγγενή πόλωση έως και 10%. Για αυτόν τον υψηλό βαθμό πόλωσης ευθύνεται η ευθυγράμμιση των σιδηρομαγνητικών κόκκων που βρίσκονται στον δίκσο του Be αστέρα με το μαγνητικό πεδίο του συμπαγούς αντικειμένου, αστέρα νετρονίων.

Σημαντικές αλλαγές με την πάροδο του χρόνου παρατηρήθηκαν τόσο στον βαθμό πόλωσης όσο και στη γωνία πόλωσης σε όλα τα τρία συστήματα. Αυτή η μεταβλητότητα υποδηλώνει την παρουσία παραμορφωμένου και ανισότροπου δίσκου, σε συμφωνία με τα θεωρητικά μοντέλα. Η υπόθεση ότι ο δίσκος γύρω από το άστρο Be μεγαλώνει ελεύθερα και γίνεται όλο και πιο παραμορφωμένος, ανισότροπος και έκκεντρος και τελικά μεταφέρει μάζα στον αστέρα νετρονίων είναι σε συμφωνία με αυτήν την εργασία. Αυτά τα ευρήματα ενισχύουν την κατανόησή μας για την αλληλεπίδραση μεταξύ αστέρων νετρονίων και δίσκων αποβολής άστρων Be σε συστήματα Be/X-ray.

Contents

List of Figures

List of Tables

Chapter 1

Introduction

1.1 X-ray Binaries

X-ray binaries are a class of binary stars that are one of the brightest sources of X-rays. X-ray binaries consist of a normal star (which is in the process of evolution so that nuclear burning is still taking place in its interior)—also called donor or optical—and a compact object such as a neutron star, a black hole or a white dwarf. The two components are relatively close, close enough that matter is transferred from the normal star onto the compact object due to the high gravitational field. The mechanism is known as accretion. Typically, potential energy is converted in to kinetic energy, which is dissipated as heat in the vicinity of the compact object. The temperature is so high that the resulting radiation is emitted in the X-rays.

1.2 Classification of X-ray Binaries

Depending on the type of compact object, we can divide the X-ray binaries into three main groups: black-holes systems, neutron star X-ray binaries and cataclysmic variables if the compact object is a white dwarf. We can further divide the black-holes systems and the neutron star X-ray binaries into High Mass X-ray Binaries (HMXBs) and Low Mass X-ray Binaries (LMXBs), depending on the spectral type of the donor (Reig, 2011).

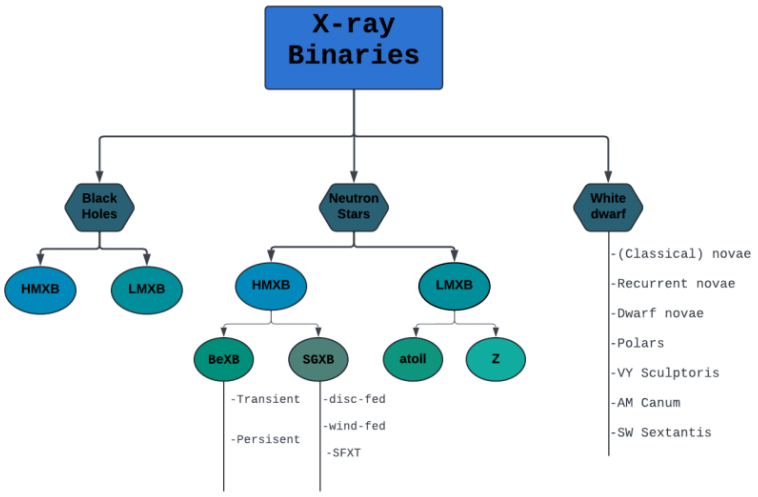

Figure 1.1: Classification of X-ray Binaries (Reig, 2011)

1.2.1 Low Mass X-ray Binaries (LMXBs)

Low Mass X-ray Binaries (LMXBs) contain a black hole or a neutron star as a compact object. The compact object is accreting from a main sequence, sub-giant or red giant star ($\leq 1\ M_{\odot}$) that is filling its Roche-lobe and thus mass transfer towards the compact object through Roche-lobe overflow. The Roche-lobe is the region around a star in a binary system within which orbiting material is gravitationally bound to that star (Fig. 1.2). The orbital period in these systems is typically of the order of hours for systems with a main sequence star and of days/weeks for systems with giants. LMXBs can be classified based on their long-term X-ray behavior into persistent systems and transient systems. Persistent LMXBs are always actively accreting while transient LMXBs exhibit large swings in their X-ray luminosity. Generally, LMXBs are considered transient if their X-ray luminosity changes by a factor of ≥ 1000. LMXBs are among the brightest X-ray sources in the sky when they

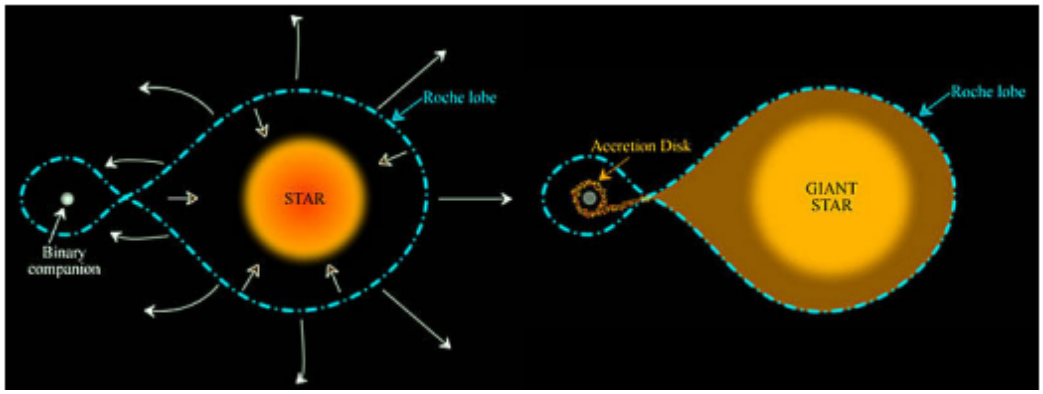

Figure 1.2: An illustration that shows the Roche lobe of the stars in a binary system.

are actively accreting. There are ≈ 200 confirmed and candidate LMXBs identified in our Galaxy. Some transient LMXBs are : KS 1731-260 , MAXI J0556-332 , Swift J1858.6-0814, and 2S 1711-339 (Bahramian and Degenaar, 2022)

1.2.2 High Mass X-ray Binaries (HMXBs)

High Mass X-ray Binaries (HMXBs) contain massive and early-type, usually O or B type, companion stars and the mass of the companion star is $\geq 10\ M_{\odot}$. The compact object in HMXBs is either a black hole or a neutron star (Fig. 1.1).
Depending on the luminosity class of the optical companion, HMXBs divide into Supergiant X-ray Binaries (SGXB) and Be/X-ray Binaries (BeXB). The former contain evolved stars (luminosity class I-II in the Yerkes system) and the latter are main-sequence or giant stars (luminosity class III-V).

1.3 Supergiant X-ray Binaries (SGXBs)

Supergiant X-ray Binaries (SGXBs) are persistent sources with luminosities around $L_x \approx 10^{36}$ erg s^{-1}, very variable on short timescales. The neutron star in SGXBs is fed by accretion from the strong radiative wind of an OB supergiant, leading to a persistent X-ray source. If mass transfer occurs via Roche-lobe overflow (Fig. 1.2) an accretion disc is formed around the neutron star. At present, there is only one known disc-fed SGXB in the Galaxy, the Cen X-3, and three in total (SMC X-1 and LMC X-4), while there are about a few tens of wind-fed SGXBs. Because SGXBs are persistent sources, they are easy to detect, and they were the first to be discovered. At first, SGXBs believed to represent the dominant population of HMXBs, so the name classical or standard was given to them, but after the INTEGRAL mission, several transient sources were discovered, making the SGXBs less numerous (Reig, 2011).

INTEGRAL mission also detect a new class of massive X-ray binaries. They are transient X-ray sources associated with O or B supergiant stars and characterized by short outbursts with very fast rise times ($\approx$ tens of minutes) and typical duration of a few hours. These sources are called Supergiant Fast X-ray Transients (SFXTs)

(Negueruela et al., 2005). The outbursts of SFXTs last for a few days and are composed of many short flares with duration of a few hours.

1.4 Be/X-ray Binaries

Be/X-ray binaries represent the largest subclass of high-mass X-ray binaries. In BeXBs, the donor is a Be star, while the compact object is, typically, a neutron star. An illustration of a Be/X-ray binary system can be seen in Fig. 1.3. Be stars are non-supergiant fast-rotating B-type (but also late O-type) and luminosity class III-IV

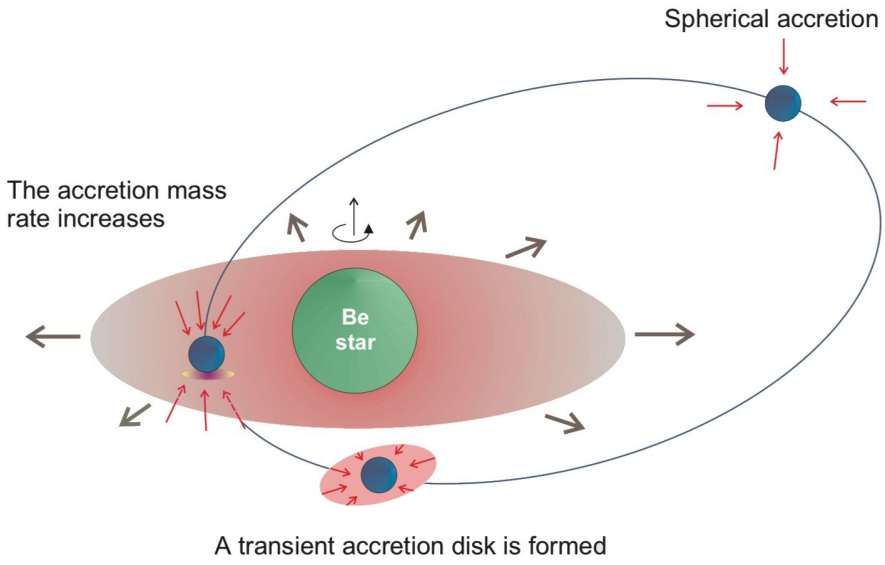

Figure 1.3: Illustration of a Be/X-ray binary system. Figure taken from Orellana and Romero (2005).

stars. The index “e” stands for "emission" and implies that Be stars have or had at some time spectral lines in emission because, compared to normal B-type stars, they are surrounded by a circumstellar disk of matter that has been ejected from the star. The causes that originate the disk are not well understood because the different mechanisms that have been proposed can not explain the observed phenomenology (Negueruela, 1998). However, Be stars are fast rotating stars, often reaching speeds close to their critical rotation velocity (the speed at which centrifugal forces at the equator balance gravitational pull) (Slettebak, 1982). This high rotation speed, together with non-radial pulsations (NRPs) is thought to drive the formation of circumstellar gas disks through the ejection of material from the star’s equator (Baade, 1999). Non-radial pulsations are oscillations where different parts of the star’s surface move in and out in phase with each other, in contrast to radial pulsations, which involve the entire star expanding and contracting uniformly. For example, see Fig. 1.4 an example of non-radial pulsations or check out the complete gif: NRPs These disks are usually disks of gas without much evidence of dust. The most common lines in emission are those of Hydrogen (Balmer lines: Hα at 6563$\AA$, Hβ at 4861$\AA$ etc), He I, metal lines Fe II and sometimes also Si II and Mg II.

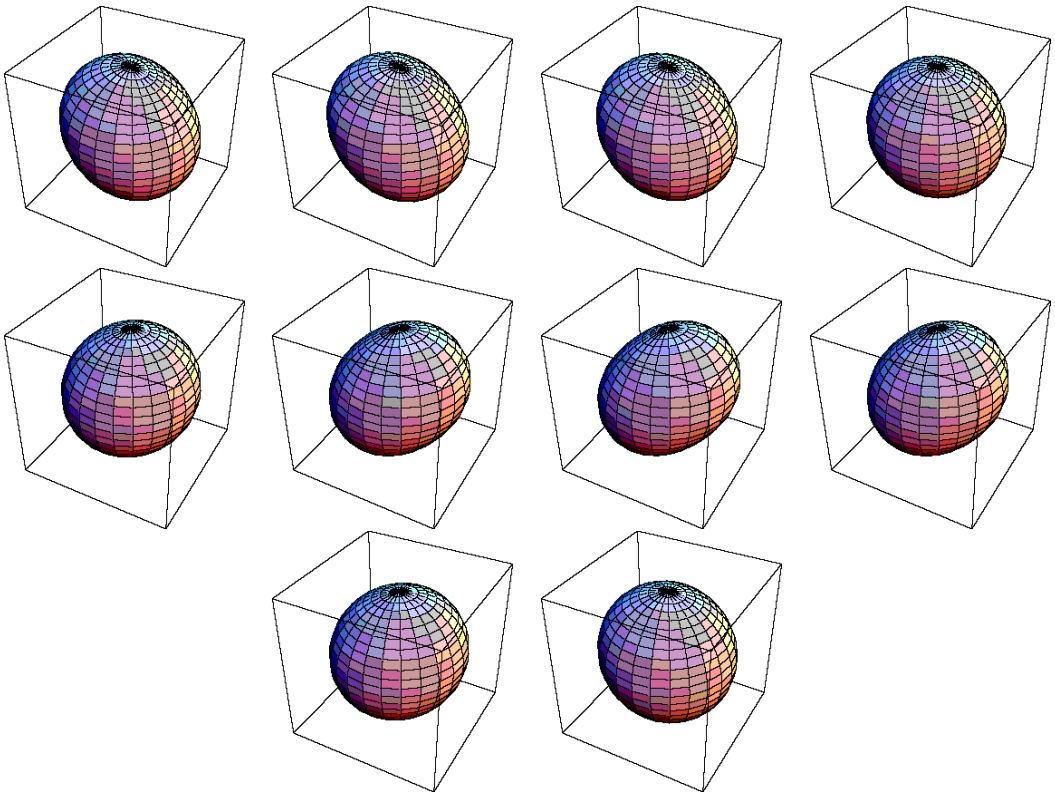

Figure 1.4: Key frames from the animation showing non-radial pulsations (NRPs)

1.4.1 X-ray Properties

Depending on the X-ray properties, there are two kinds of BeXBs: persistent X-ray emission and transient X-ray emission. Transient systems typically involve the presence of highly distorted and asymmetric discs (Martin et al., 2011, 2014). Systems with wide orbits tend to be persistent sources, accreting a low-density radial outflow and displaying no large outbursts. Systems with intermediate orbits present a mixture of both behaviours (Negueruela, 1998).
A few characteristics of persistent BeXBs are (Reig and Roche, 1999):

- low X-ray luminosity $L_{2-20keV} \approx 10^{34-35}$ erg $s^{-}1$
- all persistent sources contain slowly rotating neutron stars, $P_{spin} \geq 200$ sec.
- absence, or very weak, iron line at ≈ 6.4 keV.
- occupy wide orbit systems $P_{orb} \geq 200$ days and low-eccentric orbits ($e \leq 0.2$).

Some persistent BeXBs are : X-Per, LS I +61 235, RX J0440.9+4431, and RX J1037.5-564.
However, most BeXBs undergo outbursts in which the X-ray luminosity increases by a factor of $\geq$ 10-1000. The two types of outbursts are :

- Type I outbursts. These are regular and periodic (or quasi-periodic) outbursts, occurring close to the time of periastron passage of the neutron star (Martin et al., 2014). Type I outbursts are short, lasting for a few days reaching peak luminosities $L_x \leq 10^{37}$ erg s^{-1}.
- Type II (Giant) outbursts $L_x \geq 10^{37}$ erg s^{-1} start shortly after periastron passage and they do not show any other correlation with orbital parameters. After the X-ray outbursts, there are major changes in the physical conditions of the cirmustellar, sometimes leading to the complete disappearance of the disc

(Reig, 2011). Current theories regarding Type II outbursts suggest that these events occur when a highly misaligned disk becomes warped and eccentric, enabling the compact object companion to accrete a large amount of material (Martin et al., 2011, 2014; Okazaki et al., 2013). Detailed information about these current theories are presented in Section 1.7.

X-ray emission from BeXBs provides information on the physical conditions in the vicinity of the compact object.

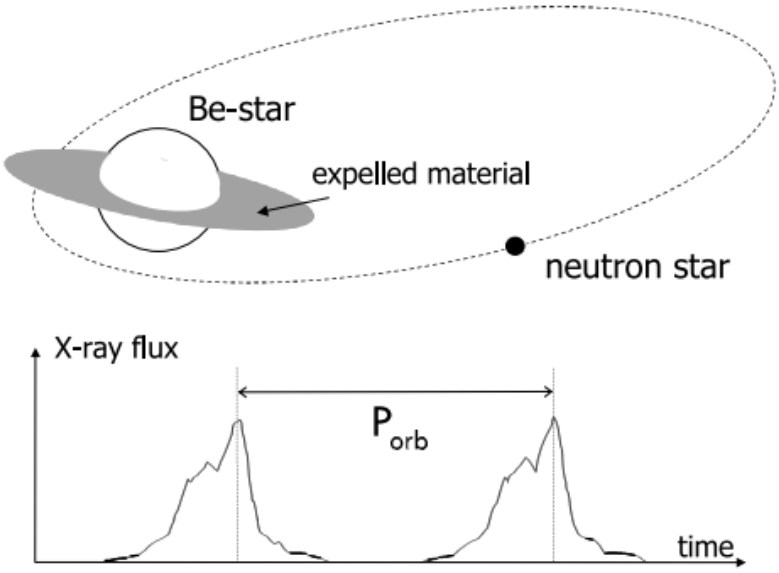

Figure 1.5: Schematic model of a Be-star X-ray binary system (Tauris & van den Heuvel 2006) (Tauris and Van Den Heuvel, 2006)

1.4.2 Optical/IR Properties

The emission spectral lines and the IR flux are two main observational characteristics of Be stars. Observations in the optical and IR help us understand the physical conditions under which the neutron star is accreting. The emission lines and the IR excess of Be star compared to the normal B-type stars that show absorption photospheric lines originate from extended circumstellar envelopes of ionized gas surrounding the equator of the Be star. As the circumstellar envelope is irradiated, photoionization and then recombination processes take place, leading to the emission of photons. The most common emission lines are those of hydrogen (Balmer lines). The strength of the emission can be variable and sometimes disappear completely, indicating that the disc has vanished. By studying the variability, we can obtain information about the geometry (size and shape) and dynamics (velocity and density laws) of the envelope.

1.4.3 Ha Line Profile and V/R Variation

Hα line is the prime indicator of the circumstellar disc state. Hα emission line can be divided into two classes: class 1 are symmetric V $\approx$ R , double-peak, wine-bottle and shell profiles Fig. 1.6 while class 2 profiles exhibit a characteristic asymmetric shape
V $\neq$ R with often a single, sometimes very sharp peak ("steeple-type") Fig. 1.7. Steeple-type profiles are variable. That means that they show asymmetric line profiles, then asymmetry inversion and re-appear with the same shape on time scales of years, also called V/R variability.

The V/R variability is defined as the ratio of the violet side (V) to the red side (R) peak intensity above continuum in units of continuum intensity (Hanuschik et al., 1995). Current models support the idea that the V/R variability is caused by global one-armed oscillations generated by differences in the density inside the equatorial disc (Okazaki, 1991). Figure 1.8 shows a schematic model of V/R variations. The grey areas in the

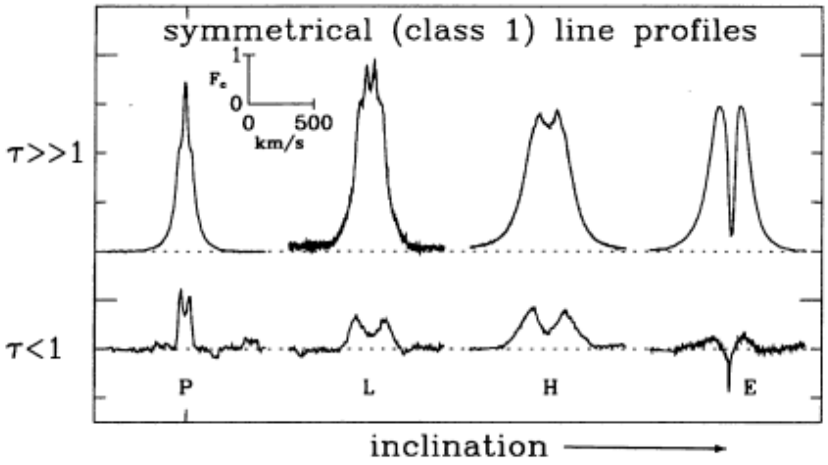

Figure 1.6: Typical emission line shapes for symmetrical (class 1) profiles (Hanuschik et al., 1995)

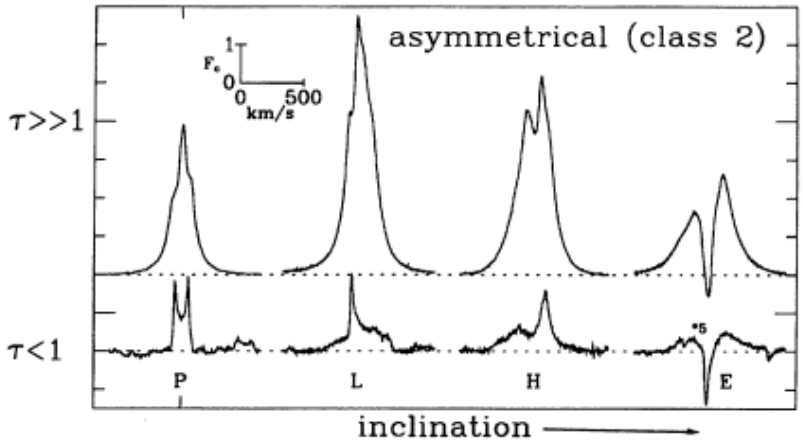

Figure 1.7: Typical emission line shapes for asymmetrical (class 2) profiles (Hanuschik et al., 1995)

disc represent the high-density part of a one-armed oscillation of the disc. Symmetric double-peak profiles are expected when the high density part is behind or in front of the star (II & IV), while asymmetric profiles are seen when the high density part is on one side of the disc (I & III). We expect to see a blue-dominated V>R profile when the high density part is moving towards the observer (I), while when the high density part is moving away from the observer (III), we expect red-dominated (V<R) profiles (Telting et al., 1994).

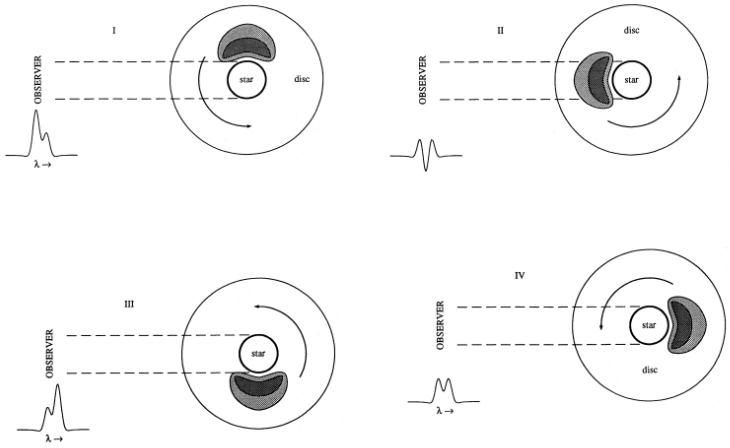

Figure 1.8: Schematic model for V/R variations (Telting et al., 1994).

1.5 Circumstellar disc

1.5.1 Disc Formation

A crucial characteristic of Be stars is that they rotate rapidly. The majority of them are found to rotate at 0.7–0.8 of their critical velocity (the velocity at which the centrifugal force at the equator is equal to the gravitational force). The determination of the rotational velocity is believed to be a crucial parameter in the formation of the circumstellar disk and can be determined by measuring the width of certain spectral lines, as it is generally assumed that the width (FWHM) of the spectral lines and the rotational velocity are linearly dependent (Steele et al., 1999). The precise mechanism that triggers the mass ejection is still not well understood. The most promising scenario that explains the formation of the disc is the non-radial pulsations (NRP) model. Non-radial pulsations may give rise to outwardly propagating circumstellar waves, which inject enough angular momentum into the upper atmosphere to spin up a Keplerian disk. Once the disc is formed, the viscous decretion disk model stands up (Rivinius et al., 2013). This model explains many of the observed features in discs around Be stars, such as the very low outflow velocities and the V/R variability.

1.5.2 Disc - Loss Episodes

Some of the Be stars can also display disc-loss episodes. As mentioned in section 1.4.3, Hα line is the prime indicator of the circumstellar disc state. When the star loses the disc, the Hα shows an absorption profile rather that emission and the X-ray activity is reduced. Because of the presence of the circumstellar disk, hydrogen free-bound and free-free emission cause the Be stars to appear redder than the non-emission B stars. So, disk-loss episodes are very important to measure the true photometric colors for the determination of the spectral type and luminosity class.

1.5.3 Disc-Neutron Star interaction

Be stars can be either part of a binary system (BeXBs) or can also exist as single objects (Porter and Rivinius, 2003; Rivinius et al., 2013). The optical/IR variability of both is generated by the equatorial disc around the star. So, any change in the variability patterns of isolated and BeXB must be the result of different structure and physical properties of the disk (size, density), since we assumed that the Be star in a BeXB and an isolated Be star have the same physical characteristics (mass, radius, luminosity). Also, considering that the main difference between an isolated Be star and a BeXB is the presence of a neutron star, any differences in the properties of the disc must be attributed to the neutron star.

The observational evidence that the neutron star affects the circumstellar disk is the correlation with the orbital

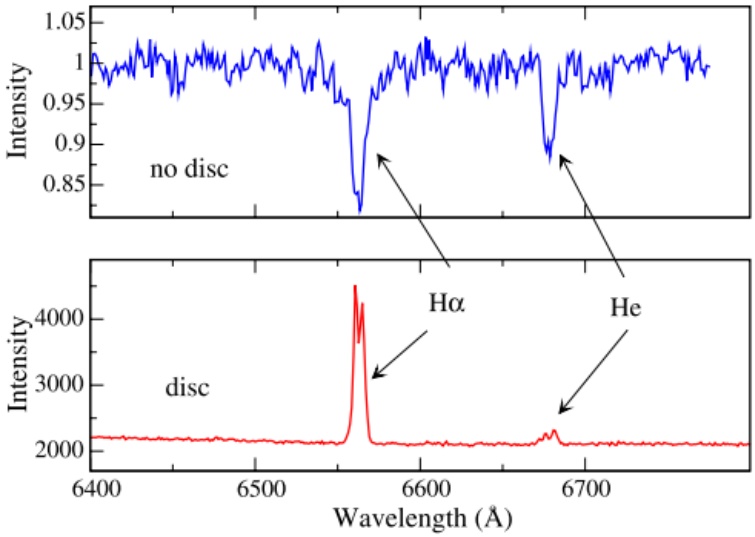

Figure 1.9: Spectrum of X Per during a disc-loss episode (up) and during the presence of the disc (down) (Reig, 2011).

period. Reig et al. (1997) found that the maximum value of the EW(Hα) has a linear correlation with the orbital period. Since the equivalent width of the Hα line represents the projected size of the circumstellar envelope, this linear correlation indicates that the neutron star plays a fundamental role in the evolution of disks in BeXBs. An updated version of the correlation between the orbital period and the EW(Hα) is shown in Fig. 1.10.

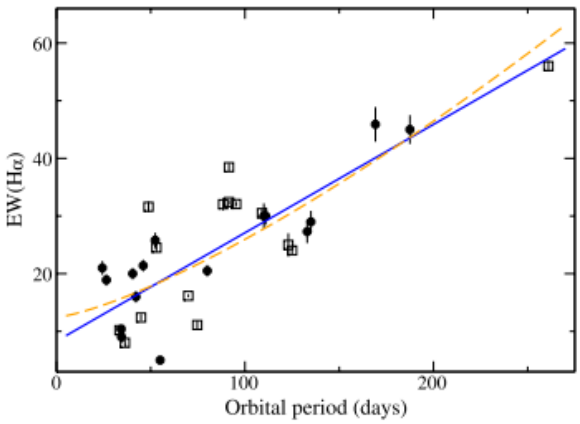

Figure 1.10: P_{orb} - EW(Hα) diagram (Reig, 2011).

Fig. 1.10 shows that in systems with short orbital periods, the number of periastron passages is larger, preventing the formation of an extended disc, while systems with longer orbital periods can develop bigger circumstellar discs and hence higher values of the EW(Hα).

Another piece of observational evidence for the effects that the neutron star produces on the circumstellar disk is the comparison of the variability patterns in isolated Be stars and BeXBs. Reig et al. (1997) compared the strength of the EW(Hα) for isolated Be stars and BeXBs and found that isolated Be stars show a larger EW(Hα) than Be stars in BeXB, meaning that isolated Be stars can develop larger disks. Also, the periods of V/R variations in isolated Be stars range from years to decades, with a statistical mean of 7 years (Okazaki, 1997). In contrast, in BeXBs, the V/R variations are shorter (< 5 years), which can be explained as the result of smaller disks due to the presence of the neutron star.

1.6 Polarization in Be/X-ray binaries

1.6.1 Thomson scattering

Thomson scattering is the elastic scattering of electromagnetic radiation by free, non-relativistic charged particles (such as electrons). The condition for Thomson scattering to apply is that the energy of the incoming photons must be much less than the rest mass energy of the electron: $\epsilon_{hv} \ll m_e c^2$ (low-energy photons). Given this condition, the charged particles will scatter the incoming light according to the principles of Thomson scattering. The mean emitted power in some direction is given by:

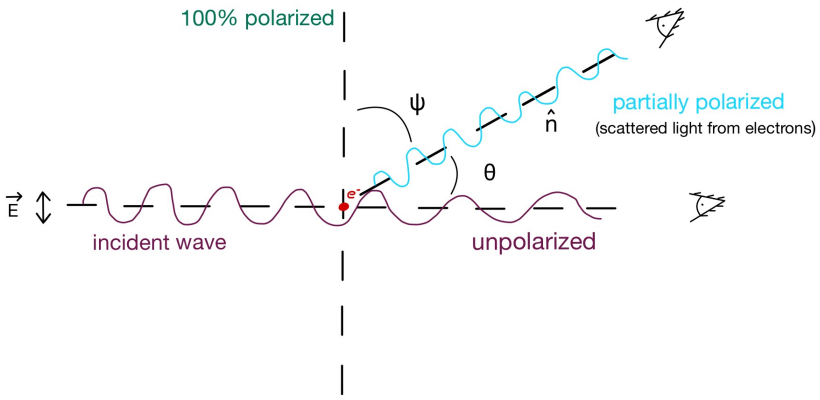

Figure 1.11: Illustration of Thomson scattering.

$$\left\langle \frac{dP}{d\Omega} \right\rangle = r_e^2 \cdot c \cdot u_{ph} \sin\psi^2 \tag{1.1}$$

where

$$r_e = \frac{e^2}{m_e c^2} \tag{1.2}$$

is the classical radius of electron,

$$u_{ph} = \frac{< E^2 >}{8\pi} + \frac{< B^2 >}{8\pi} \tag{1.3}$$

is the energy density, and ψ is the angle between the line of sight and the acceleration (the electric and magnetic components of the incident wave accelerate the particle), as seen in Fig. 1.11. The total radiative power is then:

$$P = \int \frac{dP}{d\Omega} d\Omega = \frac{8\pi}{3} r_e^2 c u_{ph} \tag{1.4}$$

where $\sigma_\tau = \frac{8\pi}{3} r_e^2$ is the Thomson scattering cross-section, which gives the probability that a photon will be scattered by an electron.
The electric and magnetic field components of the incident wave accelerate the particle. As it accelerates, it emits radiation, and thus, the wave is scattered. The scattered light can be partially polarized, depending on the scattering angle (θ). The radiation from the charged particle is $I \propto E^2$, where

$$\vec{E_{rad}} = \frac{q}{Rc^2} \hat{n} \times (\hat{n} \times \dot{\vec{u}}) \tag{1.5}$$

The polarization fraction is then defined as the ratio of the intensity of the polarized part of the scattered light I_{pol} to the total intensity of the scattered light I_{tot}:

$$p = \frac{I_{pol}}{I_{tot}} \tag{1.6}$$

The differential cross-section is:

$$\frac{d\sigma}{d\Omega} = \frac{1}{2} r_e^2 \cdot (1 + \cos\theta^2) \tag{1.7}$$

- if $\theta = 0$: no polarization
- if $\theta = 90°$: scattered light is fully polarized in 90° to the incident wave.

Thus,

$$p = \frac{1 - \cos\theta^2}{1 + \cos\theta^2} \tag{1.8}$$

The polarization of light due to Thomson scattering is always perpendicular to the plane of incidence for all scattering angles. The polarization can also be expressed in terms of the Stokes parameters $q = Q/I$ and $u = U/I$ as:

$$p = \sqrt{q^2 + u^2} \tag{1.9}$$

where I is the total intensity of the light, Q represents the difference in intensity between light polarized along the horizontal axis and the vertical axis, and U represents the difference between light polarized at 45° and -45°.

1.6.2 Polarization in Be/X-ray binaries

Polarization in Be/X-ray binaries, as well as in classical Be stars, arises due to Thomson scattering of light. Free electrons in the circumstellar disk around the Be star scatter the stellar light, leading to linear polarization (Poeckert et al., 1979; Wood et al., 1996; Yudin, 2001; Halonen et al., 2013; Haubois et al., 2014).

A detailed study by Halonen and Jones (2013) investigated the importance of gas metallicity and non-axisymmetric density distributions in the polarization of classical Be stars. They used Monte Carlo simulation to model the circumstellar environment around the Be star and computed the resulting Stokes parameters. Their findings indicate that metallicity and density perturbations significantly influence the polarization signatures of classical Be stars. The simulations reveal that non-axisymmetric density patterns cause noticeable variations in the polarization. As the high-density region rotates, it causes variations in the scattering geometry, affecting the observed polarization.

A similar study by Halonen et al. (2013) investigated the impact of optical depth on the polarization of light from circumstellar gaseous disks through non-LTE radiative transfer models. This study found that the optical depth of circumstellar disks is critical for determining the level of polarization observed. In optically thin disks, multiple scattering is negligible, whereas in optically thick disks, multiple scattering significantly modifies the polarization. As the optical depth increases, the polarization also increases and reaches a maximum around 3-4%. Beyond this range, increased optical depth causes polarization to decrease. The same authors also discussed dependence of polarization in wavelength. They mention that the observed polarization can can exhibit wavelength dependence due to dilution by unpolarized light and absorptive opacity in the disk (e.g. Figure 5 from their paper).

Three-dimensional non-LTE Monte Carlo radiative transfer models by Carciofi and Bjorkman (2006) predict that the locations in the disk where Hα photons are emitted differ from where the photons are scattered and produce polarization. Carciofi et al. (2009) showed that polarization originates mainly from the inner region of the disk (∼1-5 $R_\odot$ for Be star ζ Tauri), while Hα photons are emitted from a extended radial distance. Additionaly, Wisniewski et al. (2010) studied two Be stars, π Aquarii and 60 Cygni, using spectropolarimetric observations. They found that polarimetric and spectroscopic features do not occur simultaneously and that there is a time delay between the onset of these two (e.g see Fig. 2 in Wisniewski et al. (2010)). This observed time lag indicates that the disk-loss phase is an "inside-out" manner, meaning that the material in the inner part of the disk disperses away first.

While there are some polarimetric studies on X-ray binaries, very few are dedicated to Be/X-ray binaries and optical polarimetry of the Be star. Most polarimetric studies in Be/X-ray binaries have been focused on the compact object, which, for most of the cases, is a neutron star. As a result, there is little information available about the polarization properties of these systems.
Polarimetric studies of the Be star can give us information about the circumstellar disk dynamics and geometry. Additionally, variations in polarization over time could indicate long-term changes in the disk's state, such as

the formation or dissipation of the disk or the dynamics between the Be star and the companion star (neutron star/black hole). In Be/X-ray binaries, the companion star accretes material from the circumstellar disk of the Be star (see Fig. 1.3). This accretion results in X-ray emission (Sect. 1.4.1) and changes in the density and structure of the disk, which may affect the polarization (Roche et al., 1997). Past studies on the Be/X-ray binary GRO J2058+42 (Reig et al., 2023) found that the long-term trend in polarization supports the disk formation and dissipation cycle. Polarization decreases significantly at low optical states, when the disk is nearly gone while polarization increases as the disk reforms and becomes denser. This study also notes that during X-ray outbursts, the polarization degree shows significant variations, indicating dynamic interactions between the neutron star and the Be star's disk.

1.7 How are Type-II X-ray outbursts produced in Be/Xray binaries?

Type II X-ray outbursts in Be/X-ray binaries are intense and complex events characterized by a significant increase in the X-ray luminosity. These are thought to be triggered by interactions between the neutron star and the circumstellar decretion disk of the Be star. Many different theoretical models have been proposed to explain such events, and they are all focused on this interaction of the disk with the neutron star. Warped and precessed disks are crucial in understanding Type-II X-ray outbursts in Be/X-ray binaries. Warping is introduced by the bending or twisting of the disk out of the plane, while precession is its slow rotation around the central star. These effects are mainly gravitational in their cause, resulting from tidal forces by the neutron star companion. More specifically, tidal interactions with the neutron star—exerted by its gravitational forces, particularly if an orbit is inclined toward the disk—are responsible for complicated torques resulting in warping. This warping sets the disk into precession, thereby giving rise to significant variations in disk structure and orientation as functions of time. For instance, the theoretical models of disk instability (Negueruela and Okazaki, 2001), tidal interaction (Okazaki and Negueruela, 2001), and resonant interaction (Martin et al., 2014) are used for understanding the frameworks where warped and processed disks in Be/X-ray binaries cause Type II X-ray outbursts.

Negueruela and Okazaki (2001) attempted the above by modelling the Be/X-ray binary system 4U 0115+63—a target of our interest—focusing on understanding the properties and behavior of the circumstellar disk around the Be star. They used photometric and spectroscopic data to derive the physical parameters of the system and applied the theory of decretion disks to explain their observations. For the decretion disk model, they applied the viscous decretion disk (VDD) model as for isolated Be stars. In this model, the material ejected from the star's equatorial surface moves outward due to viscous forces, forming a disk. They discuss how the neutron star's gravitational interaction with the Be star's disk causes the disk to be truncated. Specifically, for 4U0115+63, the disk must be truncated at a resonance radius. This is determined by the orbital parameters and the viscosity of the disk material. As a result, the disk cannot extend indefinitely and constantly changes its structure, preventing it from being into a stable, steady state.

A detailed study by Okazaki et al. (2013) proposed a new scanerio to explain the origin of giant outbursts. They suggested that the Bondi-Hoyle-Lyttleton (BHL) accretion mechanism is associated with giant outbursts. *BHL accretion is the accretion process where the neutron star captures gas from an initially uniform flow of density.* After conducting three-dimensional smoothed particle hydrodynamics (SPH), they found that giant Type-II X-ray outbursts are seen in systems when the Be disk is misaligned with the binary orbital plane and sufficiently developed. When the outermost part of a warped disk intersects the neutron star's orbit near the periastron, it can capture a significant amount of gas throught BHL accretion.

Similar work by Martin et al. (2014), studied the mechanisms behind the Type-II outbursts using three-dimensional hydrodynamic simulations by modeling the long-term evolution of a Be/X-ray binary. They modelled a warped, eccentric, and precessed Be star accretion disk in order to examine how the dynamics of the disk trigger these events. They found that in order for Type-II outbursts to occur, it is necessary not only for the disk to be warped but also eccentric. They discussed that if the disk around the Be star is initially circular but inclined with respect to the orbital plane of the neutron star, then the gravitational forces that the neutron star exerts on the disk are weaker. Because gravitational forces are weaker on an inclined disk, it can grow more freely. This implies that the disk can expand until it becomes eccentric. As the disk expands and gets more eccentric, it eventually reaches a size where it may interact significantly with the neutron star, resulting in mass

transfer and an outburst. This explains why extremely misaligned disks are more likely to produce the conditions necessary for these intense events.

Both of these studies highlight the importance of the Be disk being warped and precessed, in order to trigger the outbursts.

1.8 Warped and Precessed disks: Evidence from Spectroscopic Observations

As we previously mentioned, Be stars have a decretion circumstellar disk around them. The circumstellar disk is made of matter that has been ejected from the star as a result of its high-speed rotation and non-radial pulsations. This disk is not static; over time scales from months to years, the disk of a Be star can disappear to lead to a classical B star and vice versa. Be stars show spectral lines in emission with Hα line to be the prime indicator of the circumstellar disk state. In the following figure, Fig. 1.12, we show a schematic representation of the Be star's emission line profile.

When we see the disk of a Be star on its edge, it looks like a shell around the star (C in the figure). In this

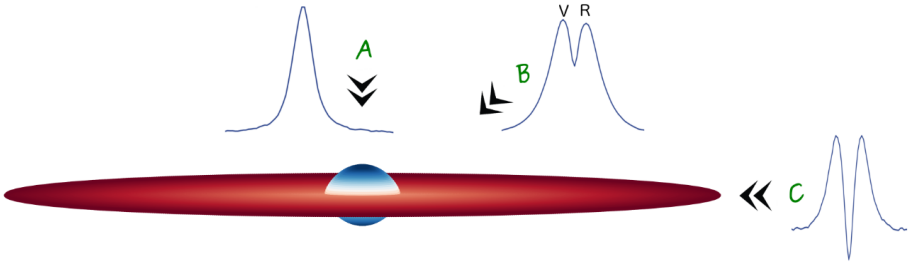

Figure 1.12: Schematic representation of emission line of Be star as seen from different inclination angle. Figure taken from here

configuration, the star is referred to as a "shell star" because it exhibits an absorption line that is narrow in nature. Line profiles of Be star disks that we observe at an intermediate inclination angle are detected to have a double peak-symmetric shape (B from the figure). Meanwhile, for the face-on disk observation, a single peak shape of the spectral lines is seen (A from the figure). The changes in line profile and spectral line shape when seen in the same star are believed to be due to the precession of the disk. Generally, the precession of a disk means that the whole misaligned disk will be slowly turning with time around the central star. This gradual variation in orientation may cause periodic changes in the observed spectral features.
Apart from precession, the Be star disks can be warped, but in warping, the deviation is the tilt of the disk. From a given plane, the parts of the disk tend to tilt at different angles, such that it leads to asymmetric and complicated line profiles, as other portions of the disk may obscure or reflect lights differently.

Past multi-wavelength studies of the Be/X-ray binary 4U0115+63 focused on the behavior of its circumstellar disk (Negueruela and Okazaki, 2001). They observed that the disk experiences quasi-cyclic formation and dissipation, as well as a variation of emission line profiles (double peaks, single peaks, shell profiles, and absorption lines), indicating considerable structural differences (e.g., fig. 2 or fig. 3 from their paper). These are all associated with disk warping and tilting episodes caused by Type II X-ray outbursts. The disk's dynamic evolution under radiation pressure from the Be star and tidal forces from the neutron star supports the hypothesis of a twisted and processed disk.

Additional spectroscopic studies of Be/X-ray binaries provide strong evidence of disk warping and precession. For example, Moritani et al. (2013) conducted high-disperion optical spectroscopy of the Be/X-ray binary A 0535+26 from the period of 2009 until 2012. Their observations covered two major outbursts and several minor ones, revealing significant variability in the Hα line profile. More specifically, Moritani et al. (2013) found two main features: a bright blue component, or blue "shoulder" (check fig. 2 from Moritani et al. (2013)), as they

say, after the periastron, which indicates a dense gas stream towards the neutron star, and a redshifted enhanced component around the 2009 giant outburst. These two features suggest that a warped and precessed disk triggered the observed X-ray outbursts.

1.9 Objectives

The most common accepted theory of what triggers the observed X-ray outbursts in Be/X-ray binaries, is that mass from the circumstellar disk of the Be star is transferred to the neutron star. However, the exact mechanism of how mass is transferred to the neutron star is still not well understood. To be more precise, the interaction between the neutron star and the decretion disk of the Be star remains a subject of debate. From an observational perspective, Type-II outbursts occur in systems with both large and small circumstellar disk, whereas there are also cases where systems with relatively large disks do not exhibit Type-II outbursts.

The disks in Be/X-ray binaries are often truncated due to the gravitational effects of the neutron star (Reig et al., 1997; Negueruela and Okazaki, 2001; Reig et al., 2016). This truncation raises the question of how substantial amounts of matter can be transferred to the neutron star to trigger the X-ray outbursts. If the disk is truncated, then accretion of large amounts of matter is only feasible if the disk becomes sufficiently asymmetric and dense to exceed the truncation radius (Martin et al., 2011, 2014; Okazaki et al., 2013).
The current theory suggests that giant outbursts occur when the neutron star captures a significant amount of gas from a warped, highly misaligned, and eccentric Be disk. Models demonstrate that such highly distorted disks can result in enhanced mass accretion when the neutron star passes through the warped region. This interaction increases the density and volume of gas available for accretion onto the neutron star, thereby triggering intense X-ray emission.

We aim to test the current theory of the warped and misaligned circumstellar disk using polarimetry. The polarization degree depends on the density of the disk, as light from the star passes through inhomogeneous regions where the scattered light exhibits different polarization characteristics depending on the local density. Additionally, the polarization angle depends on the orientation of the disk. By measuring the polarization angle, we can determine how the scattered light's polarization is oriented relative to the scattering plane, thereby inferring the orientation of the disk. Since Type-II outbursts require warped, misaligned, and eccentric disks, we expect to observe significant changes in both the polarization degree and the polarization angle.

Chapter 2

Observations & Data reduction

2.1 Observations

All the data presented in this work were obtained from the 1.3-meter telescope at the Skinakas observatory in Crete, Greece, using the RoboPol photopolarimeter [1]. The polarimeter is equipped with a 2048 x 2048 ANDOR CCD with a 13.5μm pixel size and a field of view (FOV) of 13.6 arcmin x 13.6 arcmin. All observations analyzed in this work were made with a Johnson- Cousins R-band filter and cover a time span of about ten years from 2013 to 2023. The results are shown in tables and can be found in Appendix B.

RoboPol is a four-channel optical polarimeter designed to simultaneously measure linear polarization in one sky exposure (Ramaprakash et al., 2019), avoiding possible errors caused by variations in sky conditions between measurements. RoboPol splits the incoming light into two light beams using half-wave retarders and a Wollaston prism, splitting one light beam horizontally and the other one vertically (e.g., Fig. 1 in King et al. (2014)). Thus, every point in the sky appears four times on the CCD (see Fig. 2.1), enabling RoboPol to measure simultaneously the Stokes parameters of linear polarization of all the sources in the field of view. From the horizontal plane, RoboPol measures the relative Stokes parameter

$$u = \frac{U}{I} = \frac{N_2 - N_3}{N_2 + N_3} \tag{2.1}$$

with uncertainty

$$\sigma_u = \sqrt{\frac{4(N_3^2\sigma_2^2 + N_2^2\sigma_3^2)}{(N_2 + N_3)^4}} \tag{2.2}$$

while, from the vertical plane, we obtain information about the relative Stokes parameters

$$q = \frac{Q}{I} = \frac{N_1 - N_0}{N_1 + N_0} \tag{2.3}$$

with uncertainty

$$\sigma_q = \sqrt{\frac{4(N_1^2\sigma_0^2 + N_0^2\sigma_1^2)}{(N_1 + N_0)^4}} \tag{2.4}$$

where I is the total intensity, U, and Q are the linear polarization Stokes parameters, N_i $(i = 0, 1, 2, 3)$ is the intensity for each spot, and σ_i their uncertainty.
Since every point in the sky appears four times, a mask is placed at the center of the field of view to reduce the background of the sky and increase measurement accuracy for the target of interest (e.g. Fig. 5 in Ramaprakash et al. (2019)).

[1] https://robopol.physics.uoc.gr/

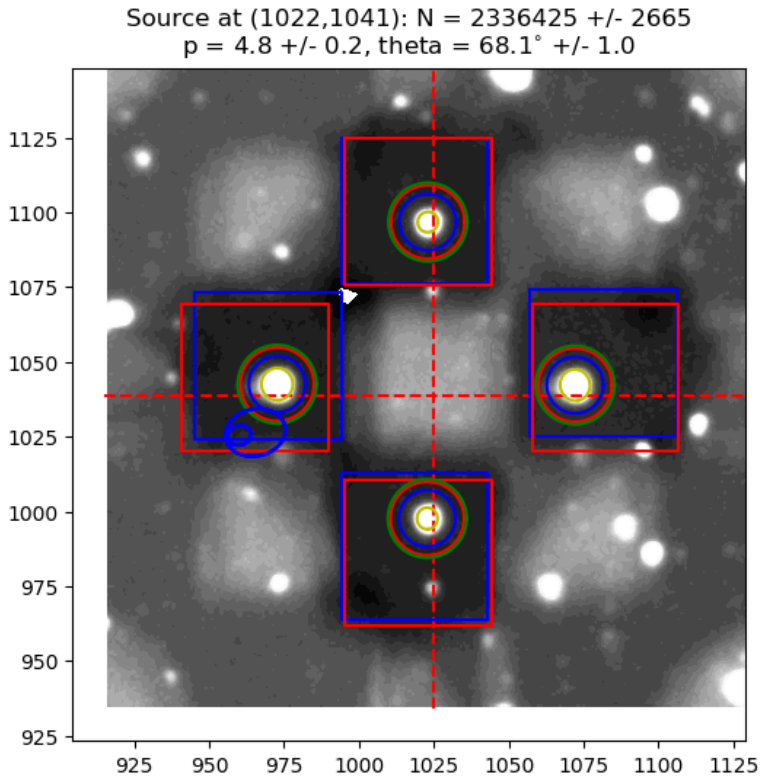

Figure 2.1: Example of a RoboPol image. For the **vertical** plane: the **top** spot is $i = 0$, while the **bottom** spot is $i = 1$. For the **horizontal** plane: the **right** spot is $i = 2$, while the **left** spot is $i = 3$. For the **circles:** The red circle defines the aperture size (i.e. the size used for photometry); the space between the red and blue circle is not in use, while the space between the blue and the green circle is used for measurements of background unless we have specified to measure the background within the squares.

2.2 Data reduction

Normalized Stokes parameters were derived with the RoboPol pipeline, as described in the work by King et al. (2014), supplemented by recent developments and improvements presented in Panopoulou et al. (2015). The pipeline is divided into five essential tools: source identification, aperture photometry, photometry correction, polarimetry, and relative photometry.

The first step of the pipeline is to identify which spot corresponds to which source. Thus, it obtains an astrometry solution using the World Coordinate System (WCS). Once the sources in the sky have been identified, the pipeline performs aperture photometry for each spot to measure the intensity and the background level. Additionally, a correction for the intensity of each measured spot, N_i in Eq. 2.1 - 2.4, is applied. Then, the linear polarization p and the electric vector position angle (EVPA or χ) are calculated according to:

$$p = \sqrt{q^2 + u^2} \tag{2.5}$$

with error:

$$\sigma_p = \sqrt{\frac{q^2\sigma_q^2 + u^2\sigma_u^2}{q^2 + u^2}} \tag{2.6}$$

and

$$\chi = \frac{1}{2} tan^{-1}\left(\frac{u}{q}\right) \tag{2.7}$$

with error:

$$\sigma_\chi = \sqrt{\frac{u^2\sigma_q^2 + q^2\sigma_u^2}{(q^2 + u^2)^2}} \tag{2.8}$$

respectively. Finally, the brightness of the sources relative to non-variable reference sources in the field is calculated.

All measurements were also corrected for instrumental polarization using standard polarimetric standards, which had to be measured regularly, according to the description in Blinov et al. (2021).

Chapter 3

Results

Below, we give the results of the analysis. We will analyze the variation of the degree of polarization (PD) and angle of polarization (EVPA) of X-rays. The list of all the targets studied in this work with their characteristics is shown in Table 3.1.

Table 3.1: List of the targets.

X-ray name	Spectral type	$P_{\rm orb}$ (d)	$P_{\rm spin}$ (s)	d(kpc)	Results[a]
KS 1947+300	B0V	40.4	18.7	9.5	B5
EXO2030+375	B0V	46.02	41.31	7	B6
4U 0115+63	B0.2V	24.3	3.61	8	B7

[a] The last column refers to the table found in the appendix that contains the results of our analysis after the correction for interstellar polarization.

More information about the individual targets can be found in Appendix A. The numerical results from our analysis (polarization degree, polarization angle, and the Stokes parameters q and u can be found in Appendix B). In Fig. 3.1, we also present our targets in a RA-Dec plot, where each star symbol represents an individual target.

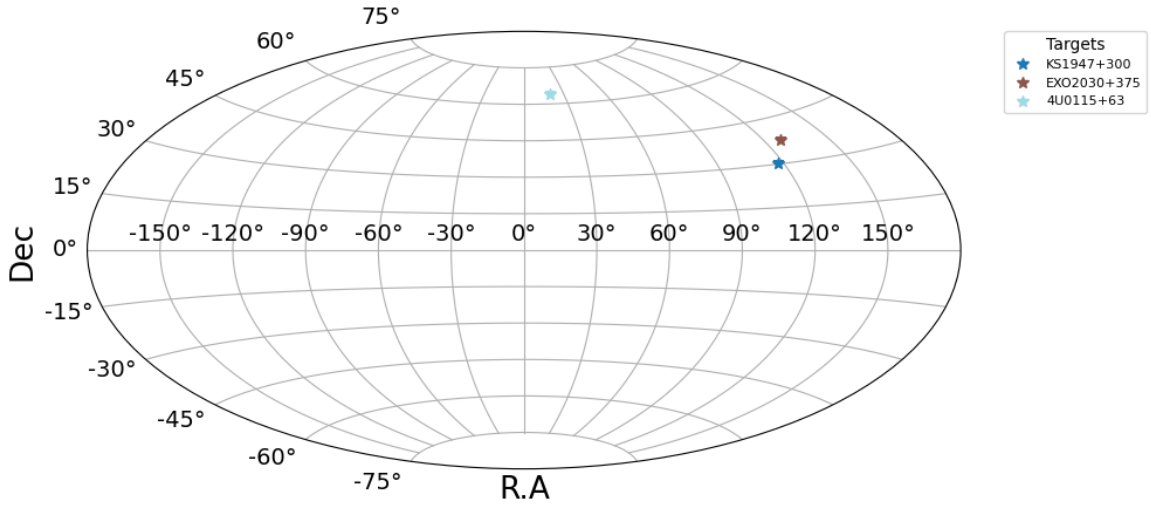

Figure 3.1: Plot showing the RA and Dec coordinates of our observed targets.

3.1 Interstellar medium correction

Here we describe how we corrected our results for polarization effects caused by the interstellar medium (ISM). Interstellar polarization (ISP) occurs when interstellar dust grains align with the Galactic magnetic field. To reduce and adjust for interstellar polarization, we employ a technique known as the "Field Star Technique." This technique requires choosing stars close to our targets that are at similar distances and ideally have negligible or zero intrinsic polarization. By measuring the polarization of the field stars, we can determine the average interstellar polarization along the line of sight. The measured Stokes u and q are then subtracted from the measured polarization of our target's interest. This technique allows us to estimate the intrinsic polarization and eliminate the contribution from interstellar polarization.

3.1.1 KS1947+300

In Fig. 3.2, we show the plot that presents the polarization measurements of the KS1947+300 over the period 2013–2023, displayed on the Stokes q-u plane. The horizontal axis represents the Stokes parameter q, and the vertical axis represents Stokes parameter u. The colored data points correspond to the average q and u values for a specific year. In the same plot, we also show the polarization measurement of the field stars we used to correct for interstellar polarization in green. The different names gfsi (i = 1, 2, 3, 4,5) correspond to different field stars. The error bars associated with each point indicate the uncertainties in the measurements of q and u. The field stars provide an estimate of the interstellar polarization along the line of sight to KS1947+300. To correct for the interstellar polarization in our target, we calculated the average values of q and u for the field stars, and then we subtracted them from the q and u values of KS1947+300. In Fig. 3.3, we show the q-u plane

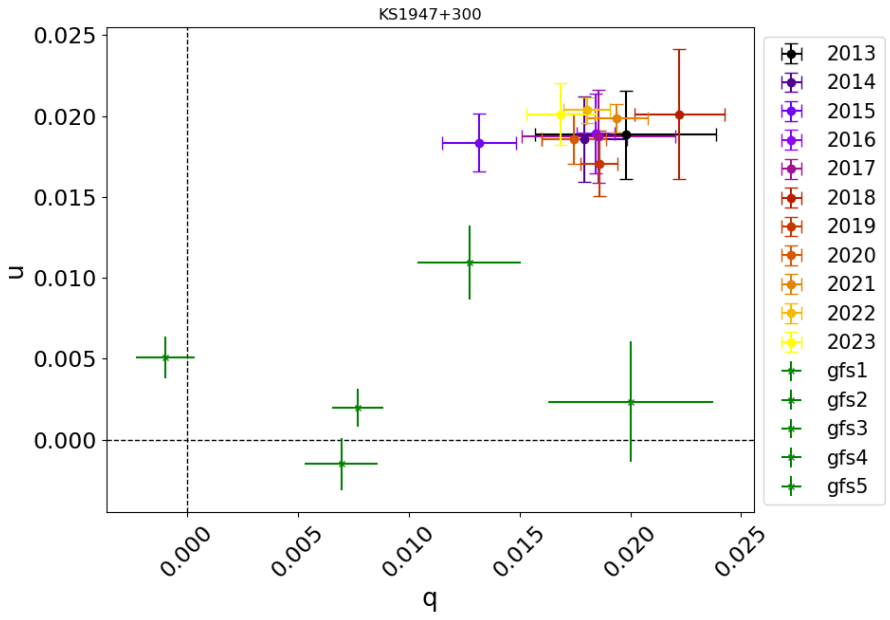

Figure 3.2: q-u plot shows the polarization measurements of KS1947+300 over several years. The plot also includes the field stars that were used for ISP correction.

after the interstellar polarization correction.

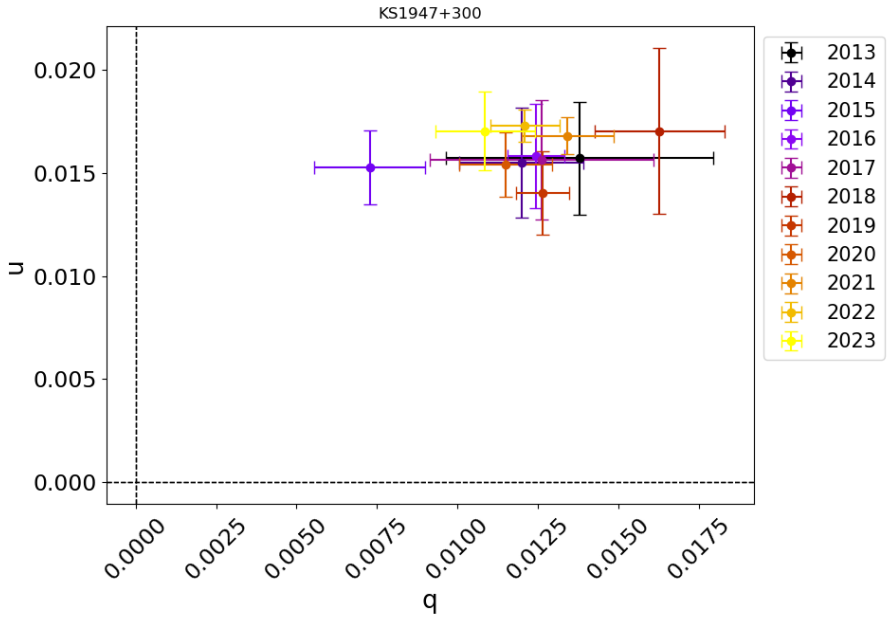

Figure 3.3: q-u plot shows the polarization of KS1947+300 after ISP correction.

3.1.2 EXO2030+375

Figure 3.4 displays the polarization data of the EXO2030+375 from 2013 to 2023 on the Stokes q-u plane. The colored data points correspond to the average q and u values for a given year, while the green data points correspond to the q and u values for the field stars. The error bars for each point show the uncertainties in the measurements of q and u. After the interstellar polarization correction, the q-u plot for EXO2030+375 is the

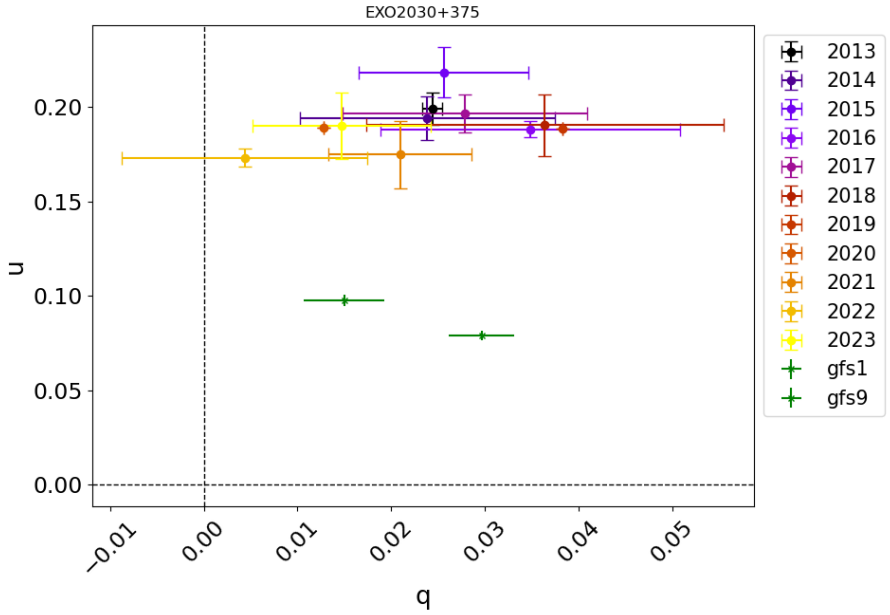

Figure 3.4: q-u plot shows the polarization measurements of EXO2030+375 over several years. The plot also includes the field stars that were used for ISP correction.

one shown in Fig. 3.5

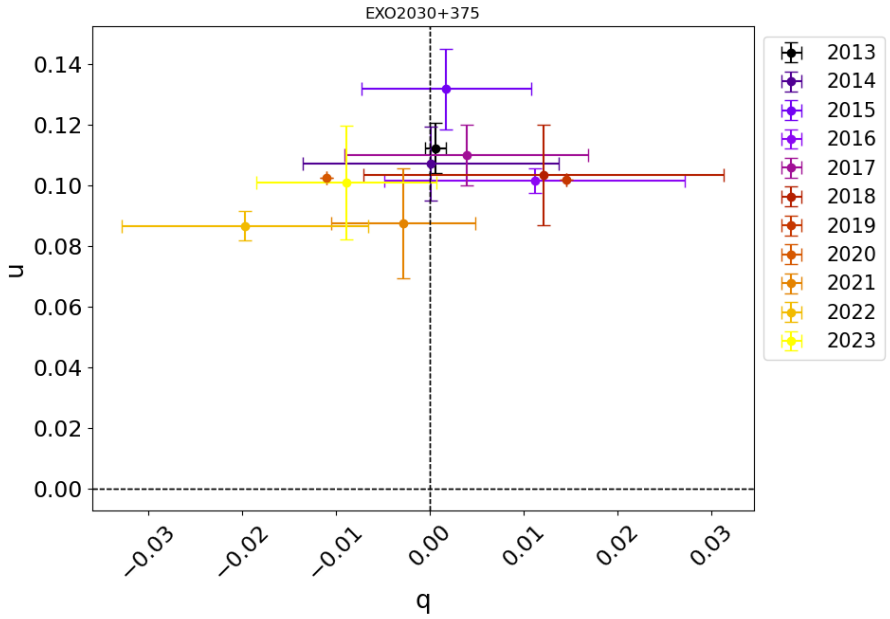

Figure 3.5: q-u plot shows the polarization of EXO2030+375 after ISP correction.

3.1.3 4U0115+63

We followed the same procedure for 4U0115+63. Figure 3.6 displays the polarization data from 2013 until 2023 without the correction for interstellar polarization. In Fig. 3.7, we show the polarization data after the field star

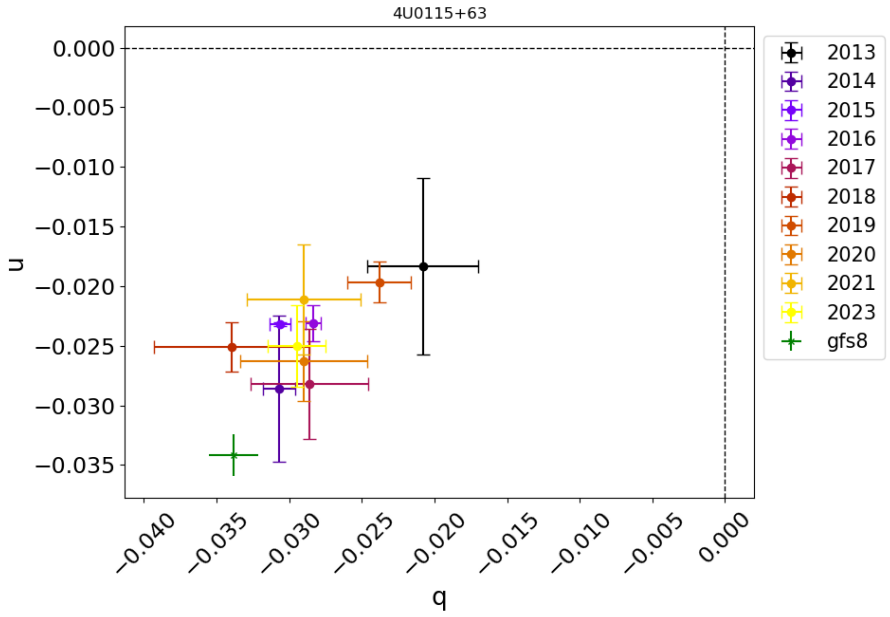

Figure 3.6: q-u plot shows the polarization measurements of 4U0115+63 over several years. The plot also includes the field stars that were used for ISP correction.

subtraction.

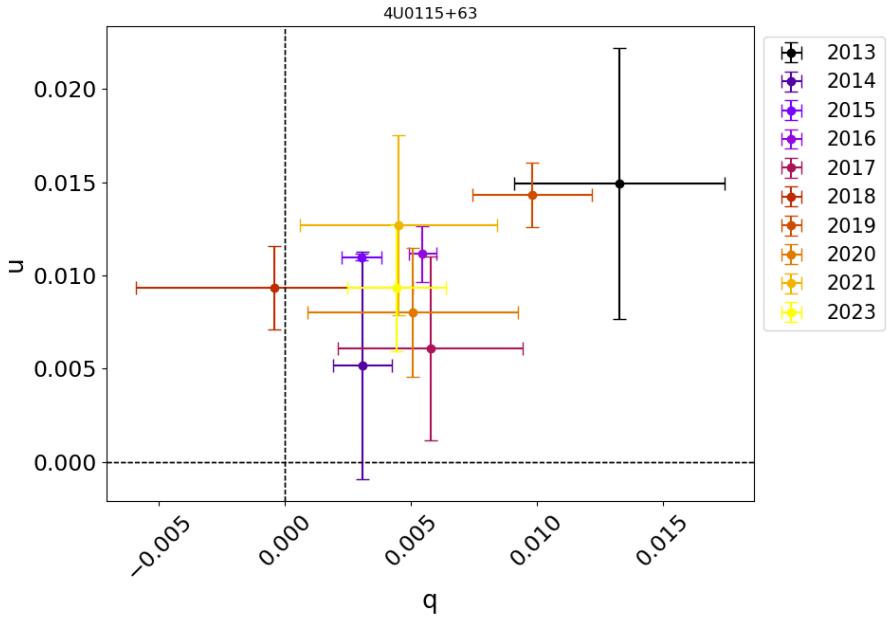

Figure 3.7: q-u plot shows the polarization of 4U0115+63 after ISP correction.

3.2 Stokes q-u parameters during X-ray outbursts

During Type II outbursts in Be/X-ray binaries, we expect to see variability in the q-u plane due to dynamic interactions between the neutron star and the Be star's circumstellar disk. These outbursts include a considerable mass transfer from the Be star's disk to the neutron star. This interaction changes the geometry and density of the disk, which influences the polarization state of the emitted light. During an outburst, the polarization parameters q and u exhibit increased variability, indicating an unstable and dynamic environment. Here in this section, we present the polarization measurements displayed on the Stokes q-u plane during the X-ray outbursts.

3.2.1 KS1947+300

KS1947+300 underwent a Type-II outburst, which was followed by three further minor outbursts (the X-ray light curve is shown in Fig. A.1). The plot of the polarization on the q-u plane throughout this period is displayed as a whole in the left panel of Fig. 3.8, and the q-u plane for each of the two different outburst phases is displayed separately in the right panel of Fig. 3.8. For the left figure: The numbers 1–30 represent ordered observations of the Stokes parameters q and u, and the error bars show measurement errors. We note that we colored the data points differently in order to enhance the visibility of changes in the q and u values more clearly. The first major outburst occurs from point 1 to point 14. From point 15, the following outbursts occur, as indicated by the corresponding X-ray light curve (Fig. A.1). To distinguish the evolution of the q and u parameters between the two outburst phases, check the right figure in Fig. 3.8).
As time passes, the data points vary, with some considerable discrepancies. At point 5, the polarization state shifts to $u \sim 0.017$ and $q \sim 0.023$, suggesting a significant change. Similarly, point 16 indicates a significant drop in the u value to approximately $u \sim 0.008$, but the q value remains close to the center. These variations in the q and u parameters represent the dynamic environment and changes within the system, maybe due to interactions between the neutron star and the Be star's circumstellar disk, which can modify the geometry and density of the disk.

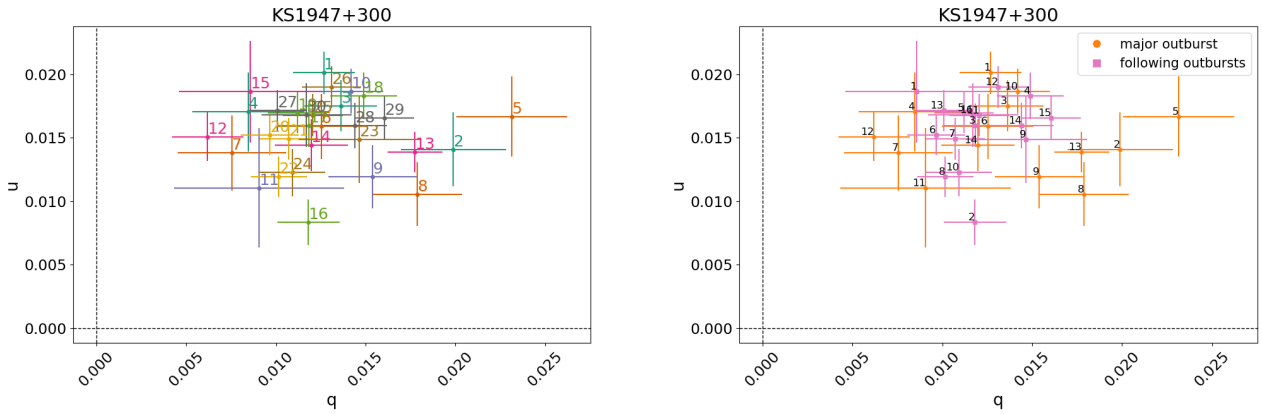

(a) q-u plot during the total 2013 X-ray outburst.

(b) q-u plot for the two distinct outburst phases.

Figure 3.8: q-u plots of KS1947+300 during the 2013 X-ray outburst.

3.2.2 EXO2030+375

EXO2030+375 underwent a Type-II outburst during 2021 (see Fig. A.2, the X-ray light curve). In Fig. 3.9, we show the plot of the polarization on the q-u plane during this period. The numbers 1–10 represent ordered

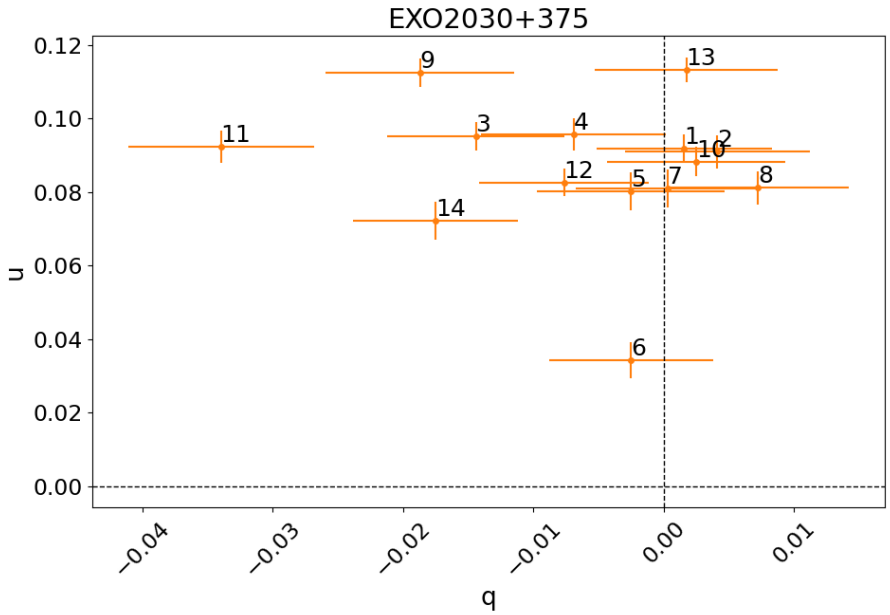

Figure 3.9: q-u plot of EXO2030+375 during the 2021 X-ray outburst.

observations of the Stokes parameters q and u, and the green error bars show measurement errors. Initially, the polarization state is about $q \sim 0.002$ and $u \sim 0.092$. As the outburst progresses, we see changes in the q and u variables. A notable change occurs at point 6, where the u value decreases to around 0.034 and the q value shifts slightly to -0.0025, indicating a temporary change in the polarization state. In general, the graph indicates that not only the polarization degree varies, but so does the polarization angle. The change in the q and u values represents the dynamic interactions between the neutron star and the Be star's circumstellar disk during the outburst, with variations in the disk's geometry and density affecting the polarization state of the emitted light.

3.2.3 4U0115+63

In Fig. A.3, we show the X-ray light curve of 4U0115+63 obtained by Swift/BAT Hard X-ray Transient Monitor. Since 2005, the Be/X-ray binary 4U0115+63 has undergone five major X-ray outbursts. During the period we observed the source (2013-2023, $\sim$ 2457000 - 2460000), 4U0115+63 underwent three main outbursts and four small ones (light blue color in the zoom panel). Below in Fig. 3.10, we plot the values of q and u for the X-ray outbursts in 2017 (JD 2457971) and in 2023 (JD 2460042). For the rest of the X-ray outbursts, we do not have sufficient data to plot. The orange points are observations from the 2017 outburst, while the pink points are from

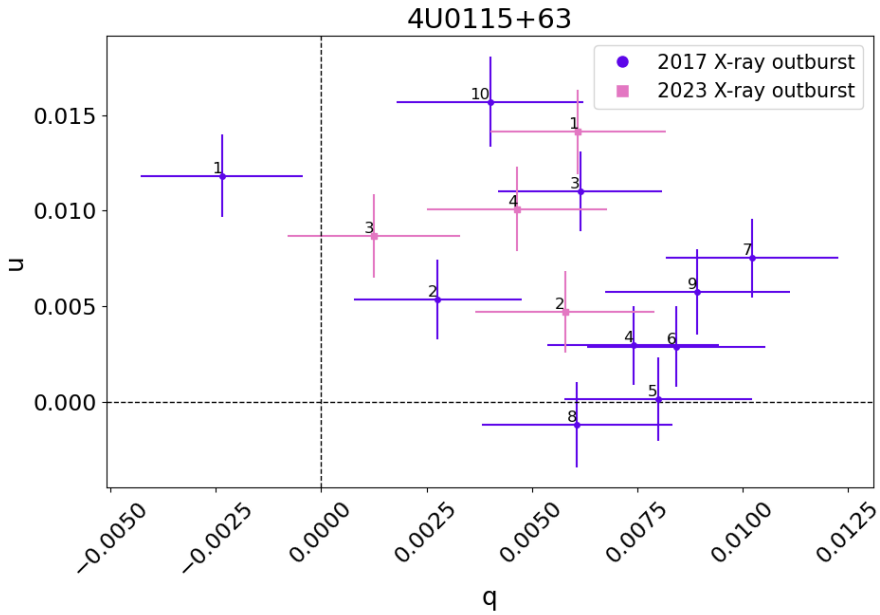

Figure 3.10: q-u plot of 4U0115+63 during the X-ray outbursts.

2023. In each case, the number indicates the measurement order for that outburst. From the 2017 outburst, most q values shift to the right, with u values oscillating between -0.0120 (point 8) and 0.0157 (point 10). Variability patterns for q and u are similar in the 2023 outburst. The q parameter varies from 0.00125 to 0.00610, while the u parameter varies from 0.00472 to 0.01412. These variations from both outbursts indicate the interactions of the neutron star with the circumstellar disk of a Be star.

3.3 Evolution of Polarization degree and Polarization Angle over time

In this section, we present the evolution plots that show the changes in polarization degree and polarization angle over time. These plots are crucial for understanding the dynamic processes occurring in the system. Variations in polarization over time could represent evidence of disk dynamics between the Be star and neutron star or of changes in the disk's formation or dissipation. Similarly, variations in polarization angle reveal changes in the orientation of the polarization vector. Variations in polarization angle may indicate warping disks and changes in the orientation of the disk relative to our line of sight.

3.3.1 KS1947+300

In the left figure of Fig. 3.11, we plot the polarization degree (PD %) of KS1947+300 over time, while in the right panel of Fig. 3.11, we show the polarization angle (EVPA) over time. The red-dashed vertical line indicates the peak of the X-ray outburst, while the red-shaded region indicates the beginning and end of this outburst. You can find the complete X-ray light curve in the appendix (Fig. A.1). The purple data points represent the measured polarization degree and polarization angle at various times, with error bars indicating the uncertainties in these measurements. We find that the polarization degree varies significantly during the X-ray outburst, ranging from

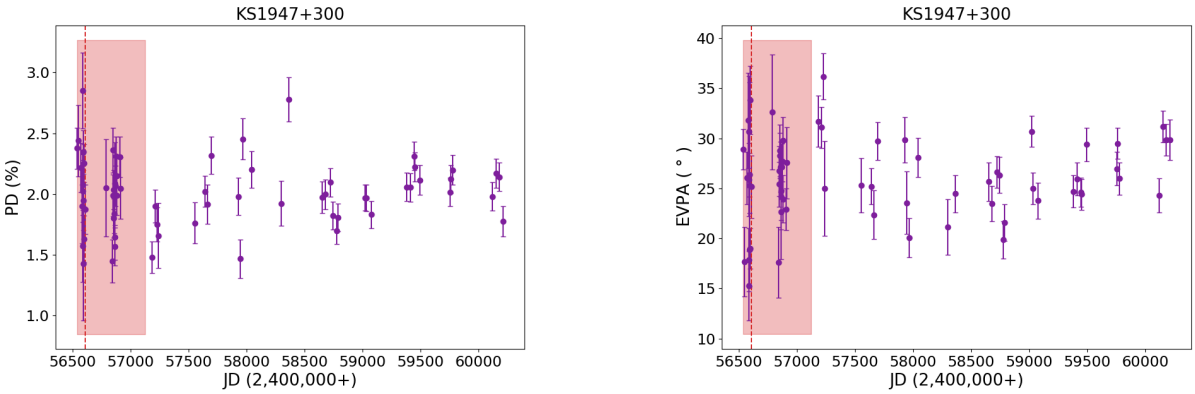

(a) Polarization degree evolution over time.

(b) Polarization angle evolution over time.

Figure 3.11: Evolution of polarization degree and polarization angle of KS1947+300 over time.

$\sim$ 2.83% to $\sim$ 1.42%. This suggests changes in the circumstellar disk, possibly related to disk formation or dissipation or the dynamics between the neutron star and the Be star. Similarly, the polarization angle decreases from $\sim 34°$ to $\sim 16°$ during the X-ray outburst. This variation denotes modifications in the polarization vector's orientation.
Both the polarization angle and the polarization degree exhibit variability during times when there are no X-ray outbursts, indicating that the disk is still active and that changes are occurring within it.

3.3.2 EXO2030+375

Figure 3.12 shows the polarization degree and angle from 2013 (JD 2456572) to 2023 (JD 2460181). In the same plots, we also illustrate the period when EXO2030+375 had a massive X-ray outburst (in 2021-JD 2459465), followed by smaller ones (Fig. A.2). During the period of the major outburst in 2021, the polarization degree remained around 9%, indicating a relatively stable polarization state. However, there are some notable deviations. For instance, there is a significant drop to 3.4% on JD 2459445, which is significantly lower than the surrounding observations. This drop indicates a brief but significant shift in the disk's structure or density, potentially due to a localized disruption. Following this drop, the polarization degree increases again, reaching values of 11.4% on JD 2459495.
Similarly, from the right panel of Fig. 3.12, we see that the polarization angle during the 2021 outburst changed almost 10°. As the outburst progresses, we observe an increase to values around $\sim 52.0°$.

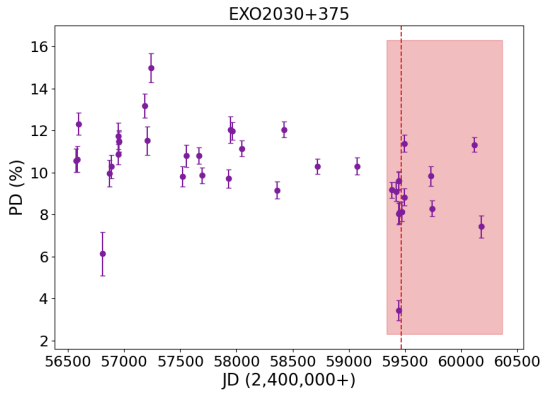

(a) Polarization degree evolution over time.

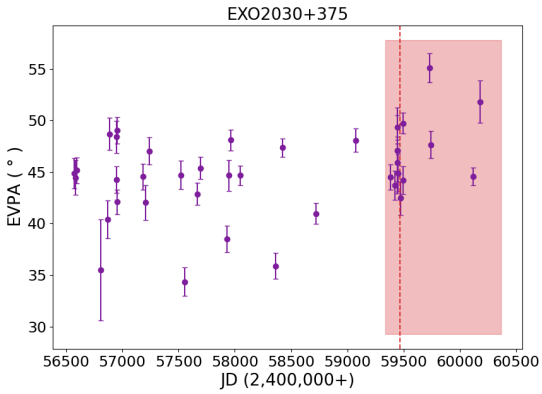

(b) Polarization angle evolution over time.

Figure 3.12: Evolution of polarization degree and polarization angle of EXO2030+375 over time.

Overall, the polarization degree and angle vary over the observing period. The light curve (Fig. A.2) shows persistent X-ray activity, which correlates with these changes. The light curve shows that EXO2030+375 has continuous X-ray activity. These outbursts could explain the observed fluctuations in polarization degree and polarization angle.

3.3.3 4U0115+63

The evolution plot of polarization degree over time for 4U0115+63 is shown in the left figure of Fig. 3.13. The purple data points represent the observed polarization degree, with error bars that indicate the uncertainties. The red vertical lines represent the period of Type-II outbursts, while the orange vertical lines denote minor X-ray outbursts. The shaded regions indicate the beginning and end of the outbursts. The X-ray light curve can be found in Fig. A.3. As we can see from the left panel, the polarization degree changes dramatically

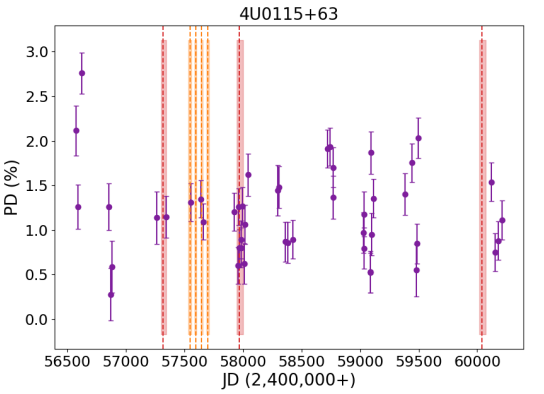

(a) Polarization degree evolution over time.

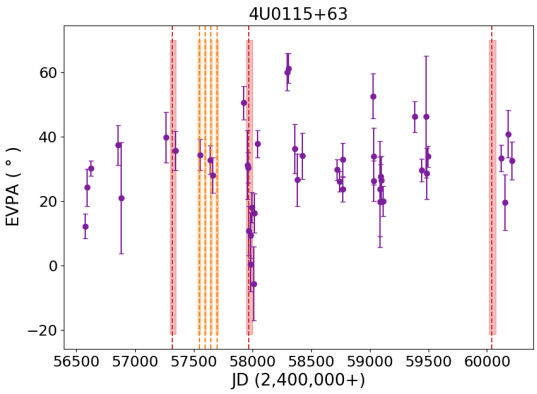

(b) Polarization angle evolution over time.

Figure 3.13: Evolution of polarization degree and polarization angle of 4U0115+63 over time.

over time, with values ranging from almost 0.0% to less than 3.0%. Significant changes in the polarization degree are observed during the Type-II outbursts (shown by the red lines), suggesting increased activity and dynamical changes caused by intensive mass transfer events in the Be star's circumstellar disk. The minor X-ray outbursts (indicated by the orange lines) also show some variations in the polarization degree, but these changes are generally less pronounced compared to the Type II outbursts.

We also see a period of changes in polarization degree between JD 2458296 and JD 2459570, even though there is no detection of X-ray outburst activity during this time. This suggests changes in the disk's structure independently of X-ray outbursts.
From the right panel of Fig. A.3, we show the evolution in polarization angle over time. During the Type-II outburst, we see that the polarization angle changed remarkably (from $\sim 51^{\circ}$ to $\sim$ - 5.7°). Fluctuations in polarization angle also occurred in periods where no significant X-ray activity was recorded. This large change in polarization angle can indicate that the entire disk is undergoing warping or tilting.

Chapter 4

Discussion

4.1 Intrinsic polarization in Be/X-ray binaries

Statistical analysis of 495 isolated Be stars (Be stars with no companion star) investigated their intrinsic polarization, projected rotational velocities, and near-far IR excesses (Yudin, 2001). The main findings of this work regarding intrinsic polarization are the following:

1. Be stars of earlier spectral types (B0-B3) show a larger scatter in their polarization values compared to later types.
2. Also, (B0-B3) spectral type Be stars have on average higher polarization values compared to later spectral types (check Fig. 2 from their paper (Yudin, 2001)).
3. For B0-B3 stars, the maximum values of intrinsic polarization are around 2%.
4. For spectral types (B3-B9), they found an upper limit for polarization for each spectral type and showed that this upper limit follows an exponential decay function:

$$PD_{max}(\%) = 0.46 + 1.74 \cdot exp\Big(- \frac{X - 1.5}{3.22}\Big) \tag{4.1}$$

   where X: is the spectral subtype number. Note: The upper limit for B0-B3 type stars does not fit this exponential curve.

In this work, we have studied Be/X-ray binary systems rather than isolated Be stars. However, it is worth comparing our findings regarding the intrinsic polarization in Be/X-ray binaries with the phenomenology of isolated Be stars in order to see if the findings by Yudin (2001) apply here as well. We have studied three Be/X-ray binaries: KS 1947+300, EXO 2030+375, and 4U 0115+63 (see Table 3.1, or Appendix A for further information about the targets). The intrinsic polarization of this sources is shown in the left panel of figures 3.11, 3.12, and 3.13, where we plotted the intrinsic polarization versus time. For the numerical values, check Appendix B.

For KS 1947+300 and 4U 0115+63, we find that the intrinsic polarization is below 2%, which is in agreement with Yudin (2001). An exception to this is the third Be/X-ray binary we studied, the EXO 2030+375. A past study from Reig et al. (2014) studied EXO 2030+375 for six epochs, between 6 October 2013 and 1 August 2014. They mention that previous infrared polarimetric studies from Norton et al. (1994) suggested that most of the measured polarization could be attributed to interstellar polarization, with only a small intrinsic component. However, the study from Reig et al. (2014) shows that interstellar polarization cannot account for the entire observed polarization, implying a significant intrinsic contribution. Reig et al. (2014) suggested that the high optical polarization may be attributed due to the alignment of ferromagnetic grains in the Be star's circumstellar disc with the neutron star's magnetic field.

For this study, we used observations for 10 years for EXO 2030+375, from 2013 until 2023. Before correcting for the interstellar polarization, the mean value we find for the polarization degree is $PD_{mean,before}(\%) =$

18.9 ± 0.3 while the maximum value we find is $PD_{max,before}(\%) = 24 \pm 2$. After correcting for interstellar polarization, we find $PD_{mean,after}(\%) = 10.1 \pm 0.3$ and $PD_{max,before}(\%) = 15 \pm 2$ [1]. This significant decrease in polarization degree after interstellar polarization correction indicates that the interstellar medium affects the observed polarization. However, even after accounting for interstellar polarization, EXO 2030+375 still exhibits a high intrinsic polarization degree, significantly higher than the typical 2% observed in many Be stars. This shows that the system has strong intrinsic polarization mechanisms, most likely caused by the alignment of ferromagnetic grains in the circumstellar disc altered by the neutron star's magnetic field. The magnetic fields of neutron stars in X-ray binaries are known to be extremely strong, often reaching up to $\sim 10^{13}$G Revnivtsev and Mereghetti (2016), which can significantly interact with the circumstellar disk, aligning ferromagnetic grains, and enhancing polarization.

4.2 Type II outbursts in BeXBs: testing theoretical models

In this section, we discuss the long-term evolution of polarization and polarization angle for the Be/X-ray binary systems we have studied. Our data cover ten years of observations, from $\sim$ September 2013 until $\sim$ September 2023. During this period, our systems also underwent Type-II outbursts. KS1947+300 underwent a major outburst during November 2013 (at the beginning of our observational data), followed by minor ones. EXO2030+375 is a persistent X-ray source that mainly shows Type-I outbursts that are associated with the periastron passage, but it also exhibits Type-II outbursts as well (i.e., a giant outburst in 2021). 4U0115+63 underwent three main outbursts (in 2015, 2017, and 2023) and four small ones (between 2015 and 2017) over our observation period. Our goal is to determine whether the observed changes in these parameters are correlated with X-ray outbursts.

For all the systems we studied, we observed significant changes in both the polarization degree and polarization angle. These fluctuations happened not only during the periods of observed X-ray outbursts but also when there was no X-ray activity. This shows that the circumstellar disks in these Be/X-ray binaries are dynamic and constantly changing. Such pattern implies that factors other than direct interactions with the neutron star play an important role in determining the disk's structure and polarization properties.

As we previously mentioned, polarization in Be/X-ray binaries occur due to Thomson scattering. In Thomson scattering, the polarization of light is always perpendicular to the plane of incidence for all scattering angles. Given that the scattered photons originate from the Be star and the circumstellar disk around the Be star serves as the scattering medium, the polarization angle is expected to be perpendicular to the plane of the disk 1.6.

With all the above, the changes in polarization degree as well as in polarization angle strongly indicate the presence of a warped and precessed disk around the Be star. Warping happens when tidal forces from the neutron star distort the disk, leading to areas with different densities and shapes. Precession, in contrast, is the slow change in the orientation of the disk's rotational axis, typically due to the gravitational pull of the neutron star. When the disk around the Be star is warped, it means that the disk is bent and twisted rather than being flat. This warping creates regions within the disk that are oriented at different angles relative to each other and to our line of sight. Because of these varying angles, light emitted from the Be star and scattered by the disk will interact with the disk's material in different ways depending on where in the disk the scattering occurs. These interactions affect the angles at which the light is scattered. As a result, different parts of the warped disk contribute to the scattering events in different ways. This leads to variations in the amount and direction of the polarized light we observe. Some regions might scatter light more efficiently or at different angles than others, causing fluctuations in the overall polarization signal. Furthermore, when the disk precesses, its orientation shifts over time, influencing how light interacts with it and how we perceive polarization. This continuous reorientation influences both the degree of polarization and the polarization angle.

In Sect. 1.7 we mention a work from Martin et al. (2014), a theoretical study focused on Type-II outbursts in Be/X-ray binaries. The findings from this work were that an initially inclined disk with respect to the orbital plane can grow freely until it gets warped and eccentric. When it reaches a size where it can interact with the neutron star, then mass from the disk is transferred to the neutron star, leading to an outburst. This theoretical

[1] The error in the mean value was calculated according to Standard Error of the Mean ($SEM = \frac{\sigma}{\sqrt{N}}$), while the error in the maximum value was calculated according to the Standard Deviation σ.

model is in agreement with the present observational work. The significant changes we find in both polarization degree and angle support the idea of an inclined disk. Even in periods of no observed major X-ray activity, changes in polarization degree and polarization angle are still observed. Again, this aligns with the belief that as the disk grows, it gets more and more warped and eccentric.

Chapter 5

Summary

Be/X-ray binaries represent the largest sub-class of high-mass X-ray binaries. In Be/X-ray binaries, the donor is a Be star, while the compact object is, in most cases, a neutron star. Be/X-ray binaries show two types of X-ray outbursts; Type-I and Type-II outbursts, and they can also be either persistent X-ray sources or transients. The first type, Type-I, is related to the periastron passage, while Type-II outbursts do not show any correlation with the orbital elements (Reig, 2011).

The exact mechanism of what triggers the observed X-ray outbursts is actually still uncertain, whereas the current theory of what initiates them is the matter from the circumstellar disk of the Be star. The main open question is how the matter is transferred to the neutron star.

Many theoretical works have investigated the mechanism behind Type-II ourbursts (Negueruela and Okazaki, 2001; Okazaki and Negueruela, 2001; Martin et al., 2011, 2014). All these works have shown that these observed giant outbursts occur when the disk of the Be star is highly warped, precessed, and eccentric. When the disk is warped, the neutron star can capture enough matter from the disk as it passes through its warped region.

A useful tool to investigate the properties of the circumstellar disk is polarimetry. In Be/X-ray binaries, polarization occurs when free electrons in the circumstellar disk around the Be star scatters the light from the Be star according to Thomson scattering (Poeckert et al., 1979; Wood et al., 1996; Yudin, 2001; Halonen et al., 2013; Haubois et al., 2014). The polarization of light due to Thomson scattering is always perpendicular to the plane of incidence, which is the circumstellar disk. The degree of polarization in Be/X-ray binaries depends on the density of the disk, while the polarization angle depends on the orientation of the disk.

However, there are relatively few polarimetric studies specifically focused on the Be star in Be/X-ray binaries. Most existing polarimetric work has either focused on classical isolated Be stars or X-ray binaries in general, not addressing this particular sub-class in detail.

In this work, we used optical polarimetry of three Be/X-ray binaries to test the current theories behind Type-II outbursts and to investigate the properties of their circumstellar disks by comparing our findings with those of classical Be stars.

The results presented here are corrected for both instrumental polarization and interestellar medium. Our results show that two out of the three Be/X-ray binaries we tested have intrinsic polarization very similar to the one from the isolated Be stars. We find that the intrinsic polarization of KS1947+300 and 4U0115+63 is below 2%, in agreement with the work from Yudin (2001) on classical Be stars. On the other hand, the third Be/X-ray binary, EXO2030+375, exhibits relatively high intrinsic polarization ($PD_{mean}(\%) = 10.1 \pm 0.3$). We attribute this to the alignment of ferromagnetic grains in the circumstellar disk with the magnetic field of the neutron star. Furthermore, for all three systems, we find significant changes in both polarization degree and polarization angle. This observed variability supports the idea of an inclined and precessed disk. Even in periods of no observed major X-ray activity, changes in polarization degree and polarization angle are still observed. This further supports the theoretical work of (Martin et al., 2011, 2014) that as the disk grows, it becomes increasingly

warped and eccentric, and eventually mass is transferred to the neutron star, which triggers the observed X-ray outbursts.

Appendices

A Targets

A.1 KS1947+300

The HMXB transient KS1947+300 was discovered in 1989, peaking a flux of 70 ± 10 in the $2 - 27$ keV range, which was later decreased to almost 10mCrab, suggesting variation of the flux Borozdin et al. (1990). The optical counterpart of KS1947+300 was identified as a B0Ve star with $V = 14.2$ located at $\sim$ 10kpc Negueruela et al. (2003). In Fig. A.1, we show the X-ray light curve obtained from the Swift-BAT X-ray transient monitor. We see that, during November 2013, the HMXB underwent an X-ray outburst with flux $\sim$ 321 mCrab at $15 - 50$ keV, followed by three more outbursts with flux less than 100mCrab.

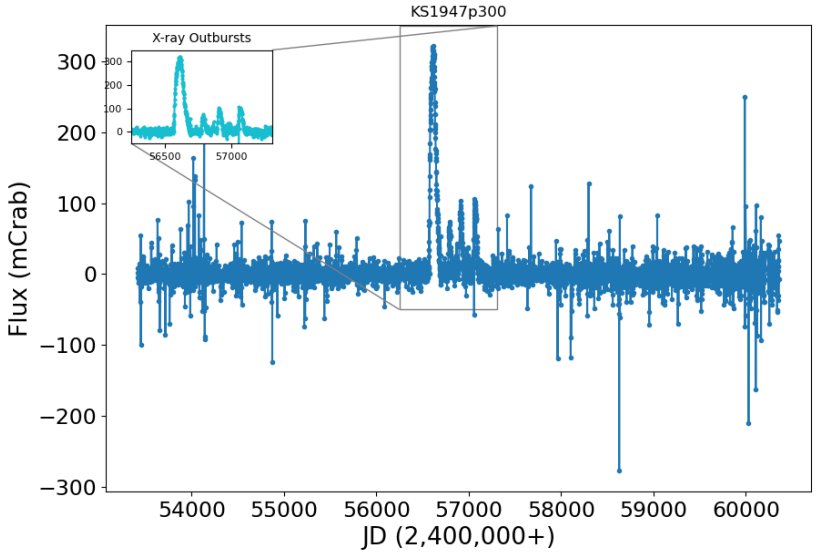

Figure A.1: X-ray activity of KS1947+300.

A.2 EXO2030+375

EXO 2030+375 was discovered during a Type-II outburst in 1985 with *EXOSAT (The European X-ray Observatory SATellite)* with X-ray pulsations of period P_{spin} =42s Parmar et al. (1989). Wilson et al. (2008) derived from Type-I outbursts orbital period equal to P_{orb} =46.02d, and they also found an eccentric orbit $e = 0.41$. In Fig. A.2, we show the X-ray activity of the HMXB EXO2030+375. EXO2030+375 is a persistent X-ray source; it shows continuous X-ray activity of Type-I outbursts similar to the zoomed plot in Fig. A.2.

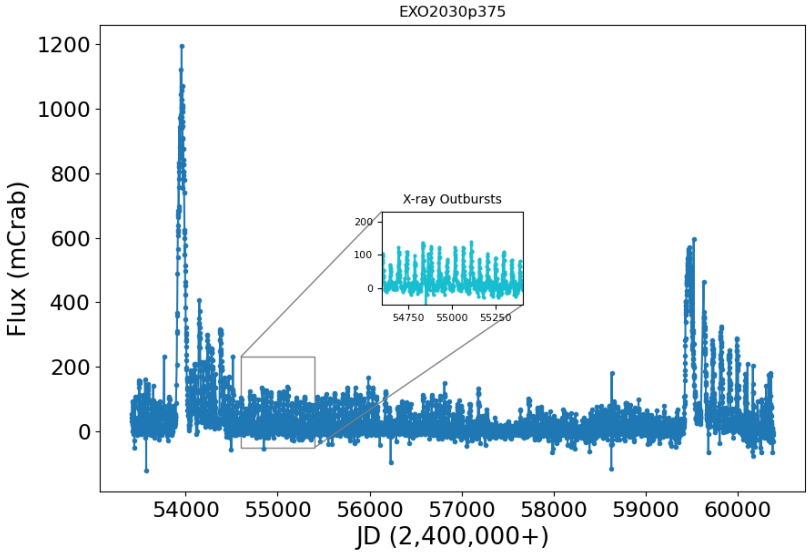

Figure A.2: X-ray activity of EXO2030+375.

A.3 4U0115+63

4U 0115+63 was detected by the UHURU satellite and first reported in Uhuru's second catalog Giacconi et al. (1972). The system consists of a neutron star with spin period P_{spin} ∼3.61s Cominsky et al. (1978). The orbital period is P_{orb} ∼24.3d and the orbit found to be eccentric with eccentricity $e = 0.34$ Rappaport et al. (1978), and a B0.2V spectral type star Johns et al. (1978) located at a distance of ∼7 kpc Negueruela and Okazaki (2001). In Fig. A.3, we show the X-ray light curve.

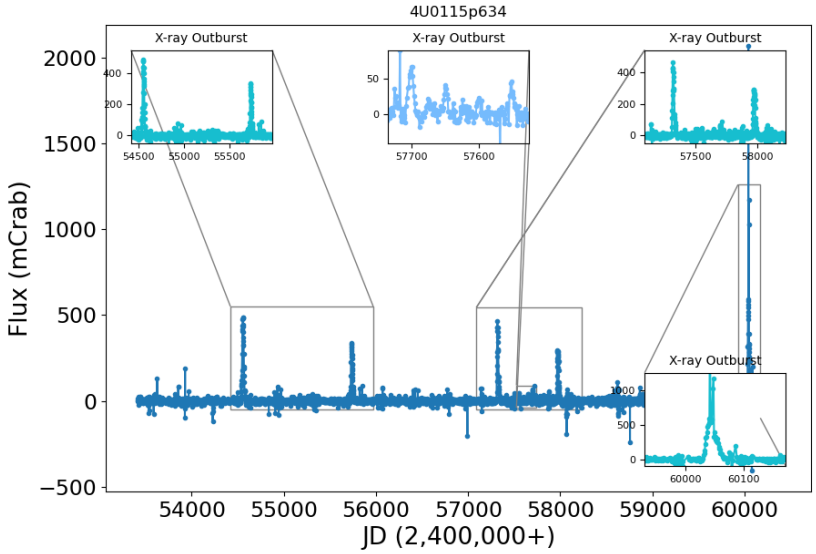

Figure A.3: X-ray activity of 4U0115+63.

B Results

In the tables below, we present the results of our analysis for all targets studied, from 2013 to 2023. The first two columns display the observation dates of each target in both the Gregorian and Julian calendars. We also include the results for polarization, the polarization angle, and the relative Stokes parameters q and u. The results are presented for each target in order as they were mentioned in Table 3.1.

B.1 Before interstellar polarization correction.

Table B1: Results for KS1947+300 (before Interstellar Polarization correction).

Date	JD (2 400 000+)	PD(%)	EVPA (°)	q	u
2013-09-01	56537.322030	2.970 ± 0.140	25.620 ± 1.360	0.0186 ± 0.0016	0.0232 ± 0.0015
2013-09-14	56550.463050	3.100 ± 0.280	16.800 ± 2.570	0.0258 ± 0.0028	0.0172 ± 0.0028
2013-10-06	56572.231290	2.840 ± 0.180	23.230 ± 1.810	0.0196 ± 0.0019	0.0206 ± 0.0019
2013-10-14	56580.243150	2.470 ± 0.300	27.190 ± 3.490	0.0144 ± 0.0031	0.0201 ± 0.0030
2013-10-20	56586.270890	3.520 ± 0.290	17.070 ± 2.410	0.0291 ± 0.0030	0.0197 ± 0.0031
2013-10-20	56586.272690	2.650 ± 0.240	22.870 ± 2.600	0.0185 ± 0.0024	0.0190 ± 0.0024
2013-10-22	56588.345120	2.160 ± 0.290	25.680 ± 3.830	0.0135 ± 0.0029	0.0169 ± 0.0029
2013-10-22	56588.346780	2.750 ± 0.240	14.880 ± 2.470	0.0238 ± 0.0024	0.0136 ± 0.0024
2013-10-24	56590.336920	2.610 ± 0.230	17.560 ± 2.550	0.0214 ± 0.0024	0.0150 ± 0.0024
2013-10-24	56590.340730	2.960 ± 0.150	23.590 ± 1.470	0.0202 ± 0.0016	0.0217 ± 0.0016
2013-10-26	56592.354150	2.060 ± 0.470	21.630 ± 6.700	0.0150 ± 0.0047	0.0141 ± 0.0046
2013-10-30	56596.349420	2.180 ± 0.170	28.100 ± 2.300	0.0121 ± 0.0018	0.0181 ± 0.0018
2013-11-02	56599.287370	2.910 ± 0.130	17.790 ± 1.230	0.0237 ± 0.0014	0.0169 ± 0.0014
2013-11-09	56606.230110	2.510 ± 0.180	22.170 ± 2.110	0.0179 ± 0.0019	0.0175 ± 0.0019
2014-05-10	56787.598310	2.610 ± 0.390	28.100 ± 4.360	0.0145 ± 0.0039	0.0217 ± 0.0040
2014-07-06	56844.553870	2.110 ± 0.160	16.360 ± 2.120	0.0178 ± 0.0016	0.0114 ± 0.0016
2014-07-08	56846.543830	2.610 ± 0.150	23.490 ± 1.620	0.0178 ± 0.0016	0.0191 ± 0.0016
2014-07-11	56850.438440	2.990 ± 0.160	22.860 ± 1.520	0.0209 ± 0.0017	0.0214 ± 0.0017
2014-07-13	56852.430750	2.640 ± 0.140	24.710 ± 1.480	0.0172 ± 0.0015	0.0200 ± 0.0014
2014-07-15	56854.438340	2.400 ± 0.140	24.750 ± 1.630	0.0156 ± 0.0014	0.0183 ± 0.0014
2014-07-19	56858.418960	2.450 ± 0.140	23.580 ± 1.600	0.0167 ± 0.0015	0.0180 ± 0.0015
2014-07-23	56862.459600	2.200 ± 0.130	21.470 ± 1.740	0.0161 ± 0.0014	0.0150 ± 0.0014
2014-07-26	56865.439010	2.730 ± 0.330	20.500 ± 3.470	0.0206 ± 0.0033	0.0179 ± 0.0033
2014-07-27	56866.491670	2.280 ± 0.160	21.140 ± 2.060	0.0169 ± 0.0017	0.0154 ± 0.0017
2014-07-30	56869.455100	2.680 ± 0.140	23.890 ± 1.490	0.0180 ± 0.0015	0.0198 ± 0.0015
2014-08-03	56873.351720	2.920 ± 0.130	24.600 ± 1.320	0.0191 ± 0.0015	0.0221 ± 0.0015
2014-08-09	56878.513840	2.580 ± 0.140	25.810 ± 1.520	0.0160 ± 0.0015	0.0202 ± 0.0014
2014-08-12	56881.516970	2.790 ± 0.150	21.530 ± 1.570	0.0204 ± 0.0016	0.0190 ± 0.0016
2014-09-04	56905.449550	2.950 ± 0.140	20.870 ± 1.340	0.0220 ± 0.0015	0.0196 ± 0.0015
2014-09-13	56914.416860	2.660 ± 0.240	24.190 ± 2.550	0.0177 ± 0.0024	0.0199 ± 0.0024
2015-06-11	57184.501280	2.060 ± 0.100	26.180 ± 1.420	0.0126 ± 0.0011	0.0163 ± 0.0011
2015-07-06	57209.541590	2.480 ± 0.100	26.650 ± 1.210	0.0148 ± 0.0012	0.0199 ± 0.0011
2015-07-24	57228.466620	2.270 ± 0.120	30.160 ± 1.450	0.0113 ± 0.0013	0.0198 ± 0.0012
2015-08-06	57240.523770	2.290 ± 0.250	21.770 ± 3.190	0.0166 ± 0.0026	0.0158 ± 0.0026
2016-06-15	57555.401050	2.390 ± 0.140	22.140 ± 1.720	0.0171 ± 0.0015	0.0167 ± 0.0015
2016-09-09	57641.242290	2.650 ± 0.090	22.370 ± 0.960	0.0188 ± 0.0010	0.0186 ± 0.0011
2016-10-03	57665.240040	2.560 ± 0.140	20.120 ± 1.510	0.0196 ± 0.0014	0.0165 ± 0.0015
2016-11-02	57695.228490	2.910 ± 0.120	26.190 ± 1.210	0.0177 ± 0.0014	0.0230 ± 0.0013
2017-06-24	57929.438690	2.570 ± 0.130	25.860 ± 1.440	0.0159 ± 0.0014	0.0202 ± 0.0014
2017-07-10	57945.376230	2.110 ± 0.130	20.480 ± 1.840	0.0159 ± 0.0014	0.0138 ± 0.0014
2017-07-30	57965.462450	3.110 ± 0.140	18.700 ± 1.270	0.0247 ± 0.0015	0.0189 ± 0.0016
2017-10-17	58044.232340	2.810 ± 0.120	24.770 ± 1.210	0.0182 ± 0.0013	0.0214 ± 0.0013

Table B1: Results for KS1947+300 (before Interstellar Polarization correction) - continued.

Date	JD (2 400 000+)	PD(%)	EVPA (°)	q	u
2018-06-28	58298.458450	2.580 ± 0.160	19.210 ± 1.800	0.0202 ± 0.0017	0.0160 ± 0.0017
2018-09-02	58364.407380	3.410 ± 0.150	22.400 ± 1.270	0.0242 ± 0.0017	0.0240 ± 0.0017
2019-06-17	58652.420420	2.600 ± 0.100	22.670 ± 1.060	0.0183 ± 0.0011	0.0185 ± 0.0011
2019-07-14	58679.391810	2.640 ± 0.080	21.050 ± 0.890	0.0196 ± 0.0010	0.0177 ± 0.0010
2019-08-25	58721.425030	2.710 ± 0.070	23.520 ± 0.760	0.0185 ± 0.0009	0.0199 ± 0.0009
2019-09-17	58744.313120	2.440 ± 0.070	22.970 ± 0.870	0.0170 ± 0.0009	0.0175 ± 0.0009
2019-10-21	58778.230810	2.350 ± 0.070	18.120 ± 0.830	0.0190 ± 0.0008	0.0139 ± 0.0009
2019-10-29	58786.194110	2.460 ± 0.070	19.460 ± 0.870	0.0191 ± 0.0009	0.0155 ± 0.0009
2020-06-19	59019.516380	2.550 ± 0.060	26.470 ± 0.670	0.0154 ± 0.0008	0.0204 ± 0.0008
2020-07-01	59031.501810	2.600 ± 0.060	22.140 ± 0.670	0.0186 ± 0.0008	0.0181 ± 0.0008
2020-08-13	59075.304480	2.470 ± 0.070	21.090 ± 0.830	0.0183 ± 0.0009	0.0166 ± 0.0009
2021-06-17	59382.557950	2.690 ± 0.070	22.010 ± 0.770	0.0193 ± 0.0009	0.0187 ± 0.0009
2021-07-17	59412.518580	2.680 ± 0.070	22.960 ± 0.780	0.0186 ± 0.0009	0.0192 ± 0.0009
2021-08-16	59443.351070	2.950 ± 0.070	22.190 ± 0.700	0.0210 ± 0.0009	0.0206 ± 0.0009
2021-08-25	59452.289530	2.860 ± 0.080	21.940 ± 0.770	0.0206 ± 0.0010	0.0198 ± 0.0010
2021-10-07	59495.223080	2.710 ± 0.090	25.690 ± 0.910	0.0169 ± 0.0011	0.0212 ± 0.0010
2022-06-25	59755.533040	2.630 ± 0.080	23.690 ± 0.830	0.0178 ± 0.0010	0.0194 ± 0.0009
2022-06-30	59761.441390	2.720 ± 0.070	25.780 ± 0.780	0.0169 ± 0.0010	0.0213 ± 0.0009
2022-07-15	59776.357410	2.820 ± 0.080	23.140 ± 0.830	0.0195 ± 0.0010	0.0204 ± 0.0010
2023-06-25	60120.509410	2.620 ± 0.070	21.630 ± 0.810	0.0191 ± 0.0009	0.0179 ± 0.0009
2023-07-27	60153.373380	2.750 ± 0.080	27.150 ± 0.850	0.0160 ± 0.0010	0.0223 ± 0.0009
2023-08-24	60181.437870	2.730 ± 0.080	26.090 ± 0.800	0.0167 ± 0.0010	0.0216 ± 0.0009
2023-09-25	60213.284070	2.370 ± 0.090	25.520 ± 1.100	0.0149 ± 0.0011	0.0184 ± 0.0010

Table B2: Results for EXO2030+375 (before Interstellar Polarization correction).

Date	JD (2 400 000+)	PD(%)	EVPA (°)	q	u
2013-10-06	56572.394490	19.410 ± 0.500	41.400 ± 0.740	0.0243 ± 0.0075	0.1925 ± 0.0051
2013-10-21	56587.405930	19.490 ± 0.580	41.190 ± 0.860	0.0258 ± 0.0080	0.1931 ± 0.0059
2013-10-29	56595.373090	21.130 ± 0.490	41.860 ± 0.670	0.0231 ± 0.0080	0.2100 ± 0.0050
2014-05-31	56808.589910	15.130 ± 0.990	36.580 ± 1.890	0.0438 ± 0.0106	0.1448 ± 0.0100
2014-08-02	56871.526220	18.940 ± 0.580	38.940 ± 0.880	0.0398 ± 0.0079	0.1852 ± 0.0060
2014-08-17	56886.557810	18.900 ± 0.520	43.390 ± 0.790	0.0106 ± 0.0076	0.1887 ± 0.0052
2014-10-16	56947.339750	20.360 ± 0.600	43.610 ± 0.840	0.0099 ± 0.0084	0.2034 ± 0.0060
2014-10-20	56951.401740	19.720 ± 0.430	41.110 ± 0.630	0.0267 ± 0.0072	0.1954 ± 0.0044
2014-10-21	56952.236270	20.070 ± 0.460	43.910 ± 0.660	0.0076 ± 0.0075	0.2005 ± 0.0046
2014-10-23	56954.375810	20.400 ± 0.410	40.000 ± 0.570	0.0355 ± 0.0071	0.2009 ± 0.0042
2015-06-11	57184.511680	22.020 ± 0.530	41.630 ± 0.690	0.0258 ± 0.0087	0.2186 ± 0.0054
2015-07-06	57209.576360	20.440 ± 0.640	39.970 ± 0.890	0.0357 ± 0.0087	0.2013 ± 0.0065
2015-08-06	57240.535050	23.660 ± 0.650	43.400 ± 0.790	0.0132 ± 0.0095	0.2363 ± 0.0066
2016-05-11	57519.567420	18.650 ± 0.420	41.170 ± 0.650	0.0248 ± 0.0069	0.1848 ± 0.0043
2016-06-15	57555.434230	19.760 ± 0.400	35.710 ± 0.580	0.0630 ± 0.0069	0.1873 ± 0.0044
2016-10-03	57665.268070	19.720 ± 0.330	40.360 ± 0.470	0.0318 ± 0.0066	0.1946 ± 0.0034
2016-11-02	57695.254310	18.670 ± 0.310	41.550 ± 0.480	0.0225 ± 0.0062	0.1854 ± 0.0032
2017-06-24	57929.456330	18.710 ± 0.340	37.940 ± 0.520	0.0456 ± 0.0063	0.1815 ± 0.0037
2017-07-10	57945.433100	20.870 ± 0.580	41.530 ± 0.800	0.0252 ± 0.0085	0.2072 ± 0.0059
2017-07-30	57965.480190	20.620 ± 0.370	43.490 ± 0.510	0.0108 ± 0.0071	0.2060 ± 0.0037
2017-10-19	58046.249110	19.990 ± 0.300	41.390 ± 0.440	0.0251 ± 0.0065	0.1983 ± 0.0031
2018-09-01	58363.429900	18.150 ± 0.270	36.600 ± 0.420	0.0525 ± 0.0057	0.1738 ± 0.0031
2018-11-03	58426.239230	20.740 ± 0.300	43.090 ± 0.420	0.0138 ± 0.0068	0.2069 ± 0.0031
2019-08-25	58721.460310	19.260 ± 0.270	39.270 ± 0.400	0.0383 ± 0.0062	0.1888 ± 0.0029
2020-08-14	59076.308500	18.970 ± 0.350	43.070 ± 0.530	0.0128 ± 0.0065	0.1893 ± 0.0035
2021-06-18	59383.539630	18.030 ± 0.320	40.960 ± 0.510	0.0254 ± 0.0061	0.1785 ± 0.0033
2021-07-27	59423.383710	17.990 ± 0.400	40.540 ± 0.630	0.0279 ± 0.0066	0.1777 ± 0.0040
2021-08-15	59442.301000	18.210 ± 0.330	43.520 ± 0.520	0.0094 ± 0.0063	0.1819 ± 0.0033
2021-08-16	59443.295720	18.320 ± 0.400	42.360 ± 0.620	0.0169 ± 0.0065	0.1825 ± 0.0040
2021-08-17	59444.336780	16.840 ± 0.470	41.370 ± 0.800	0.0213 ± 0.0066	0.1670 ± 0.0047
2021-08-18	59445.299650	12.290 ± 0.440	40.010 ± 1.030	0.0213 ± 0.0057	0.1211 ± 0.0045
2021-08-24	59451.378430	16.940 ± 0.460	40.910 ± 0.780	0.0241 ± 0.0065	0.1677 ± 0.0047
2021-09-13	59471.475170	17.070 ± 0.400	39.770 ± 0.660	0.0310 ± 0.0064	0.1679 ± 0.0040
2021-10-07	59495.302630	19.920 ± 0.330	44.270 ± 0.470	0.0051 ± 0.0067	0.1992 ± 0.0033
2021-10-08	59496.253660	17.710 ± 0.350	40.730 ± 0.560	0.0263 ± 0.0063	0.1751 ± 0.0036
2022-06-01	59732.432420	17.930 ± 0.380	46.620 ± 0.610	-0.0102 ± 0.0066	0.1790 ± 0.0038
2022-06-09	59739.502520	17.010 ± 0.310	42.280 ± 0.520	0.0162 ± 0.0059	0.1694 ± 0.0032
2023-06-24	60119.557110	20.170 ± 0.260	41.370 ± 0.370	0.0255 ± 0.0064	0.2001 ± 0.0027
2023-08-24	60181.391170	15.920 ± 0.480	43.870 ± 0.860	0.0063 ± 0.0057	0.1590 ± 0.0048

Table B3: Results for 4U0115+63 (before Interstellar Polarization correction).

Date	JD (2 400 000+)	PD(%)	EVPA (°)	q	u
2013-10-10	56576.499700	2.930 ± 0.210	-59.880 ± 2.040	-0.0145 ± 0.0022	-0.0254 ± 0.0021
2013-10-26	56592.465160	3.550 ± 0.160	-67.930 ± 1.290	-0.0255 ± 0.0018	-0.0247 ± 0.0018
2013-11-26	56623.361810	2.260 ± 0.140	-76.700 ± 1.760	-0.0203 ± 0.0014	-0.0101 ± 0.0015
2014-07-16	56854.592320	3.760 ± 0.180	-72.110 ± 1.330	-0.0305 ± 0.0019	-0.0220 ± 0.0020
2014-08-03	56872.540190	4.880 ± 0.220	-65.770 ± 1.270	-0.0324 ± 0.0024	-0.0365 ± 0.0024
2014-08-16	56885.512070	4.220 ± 0.220	-67.120 ± 1.500	-0.0295 ± 0.0023	-0.0302 ± 0.0024
2015-08-30	57264.512470	3.920 ± 0.220	-72.060 ± 1.600	-0.0318 ± 0.0023	-0.0230 ± 0.0024
2015-11-19	57346.353250	3.810 ± 0.130	-71.150 ± 0.970	-0.0302 ± 0.0014	-0.0233 ± 0.0016
2016-06-16	57555.547060	3.650 ± 0.090	-71.470 ± 0.710	-0.0291 ± 0.0011	-0.0220 ± 0.0013
2016-09-10	57641.537170	3.580 ± 0.070	-71.130 ± 0.580	-0.0283 ± 0.0010	-0.0219 ± 0.0011
2016-10-03	57665.438480	3.740 ± 0.070	-68.930 ± 0.540	-0.0278 ± 0.0010	-0.0251 ± 0.0011
2017-06-25	57929.563280	4.250 ± 0.060	-74.140 ± 0.410	-0.0362 ± 0.0009	-0.0224 ± 0.0012
2017-07-22	57957.476750	4.240 ± 0.060	-68.550 ± 0.430	-0.0310 ± 0.0011	-0.0288 ± 0.0011
2017-07-31	57966.495730	3.610 ± 0.070	-70.030 ± 0.550	-0.0277 ± 0.0010	-0.0232 ± 0.0011
2017-08-05	57970.560680	4.090 ± 0.070	-65.100 ± 0.470	-0.0264 ± 0.0011	-0.0312 ± 0.0010
2017-08-20	57985.615250	4.270 ± 0.110	-63.570 ± 0.710	-0.0258 ± 0.0014	-0.0341 ± 0.0013
2017-08-21	57986.539090	4.030 ± 0.090	-64.510 ± 0.630	-0.0254 ± 0.0013	-0.0313 ± 0.0012
2017-08-29	57994.595020	3.560 ± 0.080	-65.740 ± 0.670	-0.0236 ± 0.0011	-0.0267 ± 0.0011
2017-09-18	58015.483720	4.500 ± 0.110	-64.050 ± 0.700	-0.0277 ± 0.0015	-0.0354 ± 0.0014
2017-09-24	58020.547200	3.780 ± 0.110	-65.580 ± 0.850	-0.0249 ± 0.0014	-0.0284 ± 0.0014
2017-10-17	58043.523370	3.510 ± 0.130	-74.100 ± 1.080	-0.0298 ± 0.0014	-0.0185 ± 0.0016
2018-06-30	58299.575500	4.650 ± 0.200	-76.090 ± 1.220	-0.0411 ± 0.0021	-0.0217 ± 0.0023
2018-07-09	58308.543110	4.710 ± 0.110	-76.270 ± 0.670	-0.0418 ± 0.0013	-0.0217 ± 0.0016
2018-09-02	58363.586450	4.060 ± 0.100	-70.160 ± 0.720	-0.0312 ± 0.0013	-0.0259 ± 0.0014
2018-09-25	58386.506880	3.960 ± 0.130	-68.200 ± 0.910	-0.0287 ± 0.0015	-0.0273 ± 0.0015
2018-11-02	58425.351120	4.000 ± 0.090	-69.840 ± 0.670	-0.0305 ± 0.0012	-0.0259 ± 0.0013
2019-08-24	58720.485150	2.990 ± 0.100	-71.870 ± 0.970	-0.0241 ± 0.0011	-0.0177 ± 0.0012
2019-09-17	58743.555710	2.900 ± 0.110	-69.670 ± 1.060	-0.0220 ± 0.0012	-0.0189 ± 0.0013
2019-10-12	58769.422840	3.110 ± 0.120	-67.910 ± 1.130	-0.0223 ± 0.0014	-0.0217 ± 0.0014
2019-10-14	58771.482260	3.560 ± 0.140	-71.210 ± 1.160	-0.0282 ± 0.0016	-0.0217 ± 0.0017
2020-07-01	59031.568260	4.410 ± 0.100	-72.830 ± 0.650	-0.0364 ± 0.0012	-0.0249 ± 0.0015
2020-07-04	59034.557190	4.090 ± 0.120	-69.500 ± 0.830	-0.0308 ± 0.0014	-0.0268 ± 0.0015
2020-07-06	59036.570860	3.640 ± 0.160	-68.540 ± 1.280	-0.0267 ± 0.0017	-0.0248 ± 0.0019
2020-08-29	59090.550170	4.290 ± 0.110	-67.000 ± 0.710	-0.0298 ± 0.0014	-0.0309 ± 0.0014
2020-08-29	59090.556930	4.280 ± 0.130	-67.490 ± 0.870	-0.0303 ± 0.0016	-0.0303 ± 0.0016
2020-09-03	59095.549790	2.990 ± 0.150	-70.460 ± 1.410	-0.0232 ± 0.0015	-0.0188 ± 0.0017
2020-09-06	59098.502950	3.870 ± 0.140	-68.300 ± 1.040	-0.0281 ± 0.0016	-0.0266 ± 0.0016
2020-09-25	59117.570840	3.460 ± 0.110	-66.330 ± 0.900	-0.0234 ± 0.0013	-0.0254 ± 0.0013
2021-06-19	59384.558510	3.990 ± 0.110	-74.800 ± 0.820	-0.0344 ± 0.0013	-0.0202 ± 0.0015
2021-08-16	59442.506320	3.130 ± 0.110	-71.220 ± 1.000	-0.0248 ± 0.0012	-0.0191 ± 0.0013
2021-09-23	59480.588740	4.450 ± 0.210	-69.940 ± 1.340	-0.0341 ± 0.0022	-0.0287 ± 0.0023
2021-09-27	59484.511070	3.980 ± 0.110	-68.600 ± 0.820	-0.0292 ± 0.0014	-0.0271 ± 0.0014
2021-10-07	59495.416280	3.030 ± 0.120	-74.780 ± 1.150	-0.0261 ± 0.0013	-0.0153 ± 0.0014
2023-06-26	60121.562450	3.420 ± 0.100	-72.050 ± 0.870	-0.0277 ± 0.0012	-0.0201 ± 0.0013
2023-07-28	60153.562060	4.070 ± 0.090	-66.780 ± 0.640	-0.0280 ± 0.0013	-0.0295 ± 0.0012
2023-08-25	60181.543830	4.130 ± 0.090	-70.970 ± 0.600	-0.0326 ± 0.0011	-0.0255 ± 0.0013
2023-09-25	60213.410710	3.780 ± 0.110	-70.210 ± 0.810	-0.0291 ± 0.0013	-0.0241 ± 0.0014

B.2 Field stars.

Table B4: Field stars.

Source	Date	JD (2 400 000+)	PD(%)	EVPA (°)	q	u
KS1947+300 gfs1	2022-07-16	2459777.47401	0.52 ± 0.13	50.55 ± 7.43	-0.00100 ± 0.00133	0.00510 ± 0.00129
KS1947+300 gfs2	2022-07-16	2459777.49578	2.02 ± 0.37	3.33 ± 5.43	0.02002 ± 0.00373	0.00234 ± 0.00372
KS1947+300mgfs3	2023-07-28	2460154.45482	1.68 ± 0.23	20.34 ± 3.97	0.01273 ± 0.00234	0.01094 ± 0.00230
KS1947+300 gfs4	2023-07-28	2460154.47465	0.71 ± 0.16	-6.09 ± 6.85	0.00695 ± 0.00164	-0.00150 ± 0.00159
KS1947+300 gfs5	2023-07-29	2460155.43959	0.79 ± 0.12	7.21 ± 4.23	0.00770 ± 0.00116	0.00198 ± 0.00115
EXO2030+375 gfs1	2023-07-29	2460154.51380	9.89 ± 0.32	40.64 ± 0.91	0.01499 ± 0.00431	0.09772 ± 0.00318
EXO2030+375 gfs9	2023-08-24	2460181.46767	8.45 ± 0.25	34.73 ± 0.86	0.02964 ± 0.00351	0.07909 ± 0.00267
4U0115+63 gfs8	2021-09-27	2459484.61160	4.81 ± 0.14	-67.34 ± 0.84	-0.03381 ± 0.00170	-0.03418 ± 0.00176

B.3 After interstellar polarization correction.

Table B5: Results for KS1947+300 (after Interstellar Polarization correction).

Date	JD (2 400 000+)	PD(%)	EVPA (°)	q	u
2013-09-01	56537.322030	2.377 ± 0.169	28.889 ± 2.040	0.0127 ± 0.0017	0.0201 ± 0.0017
2013-09-14	56550.463050	2.438 ± 0.293	17.653 ± 3.471	0.0199 ± 0.0029	0.0141 ± 0.0029
2013-10-06	56572.231290	2.218 ± 0.202	26.056 ± 2.618	0.0136 ± 0.0020	0.0175 ± 0.0020
2013-10-14	56580.243150	1.902 ± 0.310	31.786 ± 4.756	0.0085 ± 0.0031	0.0170 ± 0.0031
2013-10-20	56586.270890	2.852 ± 0.311	17.867 ± 3.144	0.0232 ± 0.0031	0.0167 ± 0.0032
2013-10-20	56586.272690	2.024 ± 0.255	25.866 ± 3.649	0.0125 ± 0.0026	0.0159 ± 0.0026
2013-10-22	56588.345120	1.574 ± 0.297	30.660 ± 5.541	0.0076 ± 0.0030	0.0138 ± 0.0030
2013-10-22	56588.346780	2.078 ± 0.250	15.272 ± 3.487	0.0179 ± 0.0025	0.0106 ± 0.0025
2013-10-24	56590.336920	1.949 ± 0.247	18.889 ± 3.672	0.0154 ± 0.0025	0.0119 ± 0.0025
2013-10-24	56590.340730	2.345 ± 0.178	26.360 ± 2.181	0.0142 ± 0.0018	0.0187 ± 0.0018
2013-10-26	56592.354150	1.429 ± 0.472	25.318 ± 10.246	0.0091 ± 0.0047	0.0111 ± 0.0047
2013-10-30	56596.349420	1.630 ± 0.192	33.812 ± 3.414	0.0062 ± 0.0020	0.0151 ± 0.0019
2013-11-02	56599.287370	2.253 ± 0.156	18.998 ± 1.987	0.0177 ± 0.0015	0.0139 ± 0.0016
2013-11-09	56606.230110	1.875 ± 0.203	25.156 ± 3.130	0.0120 ± 0.0020	0.0144 ± 0.0020
2014-05-10	56787.598310	2.050 ± 0.401	32.624 ± 5.749	0.0086 ± 0.0040	0.0186 ± 0.0040
2014-07-06	56844.553870	1.447 ± 0.176	17.597 ± 3.524	0.0118 ± 0.0017	0.0083 ± 0.0018
2014-07-08	56846.543830	1.989 ± 0.172	26.727 ± 2.486	0.0118 ± 0.0017	0.0160 ± 0.0017
2014-07-11	56850.438440	2.360 ± 0.184	25.419 ± 2.244	0.0149 ± 0.0019	0.0183 ± 0.0018
2014-07-13	56852.430750	2.034 ± 0.162	28.271 ± 2.295	0.0112 ± 0.0016	0.0170 ± 0.0016
2014-07-15	56854.438340	1.801 ± 0.161	28.789 ± 2.572	0.0097 ± 0.0016	0.0152 ± 0.0016
2014-07-19	56858.418960	1.837 ± 0.162	27.124 ± 2.545	0.0107 ± 0.0016	0.0149 ± 0.0016
2014-07-23	56862.459600	1.567 ± 0.158	24.758 ± 2.912	0.0102 ± 0.0016	0.0119 ± 0.0016
2014-07-26	56865.439010	2.086 ± 0.341	22.670 ± 4.764	0.0147 ± 0.0034	0.0148 ± 0.0034
2014-07-27	56866.491670	1.643 ± 0.184	24.146 ± 3.244	0.0109 ± 0.0018	0.0123 ± 0.0019
2014-07-30	56869.455100	2.066 ± 0.165	27.134 ± 2.303	0.0121 ± 0.0017	0.0168 ± 0.0016
2014-08-03	56873.351720	2.308 ± 0.163	27.685 ± 2.028	0.0131 ± 0.0016	0.0190 ± 0.0016
2014-08-09	56878.513840	1.988 ± 0.162	29.777 ± 2.346	0.0101 ± 0.0016	0.0171 ± 0.0016
2014-08-12	56881.516970	2.150 ± 0.178	23.947 ± 2.379	0.0144 ± 0.0018	0.0159 ± 0.0018
2014-09-04	56905.449550	2.306 ± 0.167	22.935 ± 2.077	0.0160 ± 0.0016	0.0165 ± 0.0017
2014-09-13	56914.416860	2.047 ± 0.252	27.548 ± 3.565	0.0117 ± 0.0025	0.0168 ± 0.0025
2015-06-11	57184.501280	1.479 ± 0.131	31.693 ± 2.544	0.0066 ± 0.0013	0.0132 ± 0.0013
2015-07-06	57209.541590	1.899 ± 0.135	31.091 ± 2.045	0.0089 ± 0.0014	0.0168 ± 0.0013
2015-07-24	57228.466620	1.750 ± 0.140	36.159 ± 2.312	0.0053 ± 0.0014	0.0167 ± 0.0014
2015-08-06	57240.523770	1.657 ± 0.267	24.991 ± 4.708	0.0106 ± 0.0027	0.0127 ± 0.0027
2016-06-15	57555.401050	1.762 ± 0.168	25.303 ± 2.741	0.0112 ± 0.0017	0.0136 ± 0.0017
2016-09-09	57641.242290	2.020 ± 0.127	25.206 ± 1.804	0.0129 ± 0.0013	0.0156 ± 0.0013
2016-10-03	57665.240040	1.914 ± 0.162	22.357 ± 2.436	0.0136 ± 0.0016	0.0135 ± 0.0016
2016-11-02	57695.228490	2.317 ± 0.153	29.698 ± 1.896	0.0118 ± 0.0016	0.0199 ± 0.0015
2017-06-24	57929.438690	1.980 ± 0.155	29.860 ± 2.257	0.0100 ± 0.0016	0.0171 ± 0.0015
2017-07-10	57945.376230	1.467 ± 0.159	23.556 ± 3.127	0.0100 ± 0.0016	0.0107 ± 0.0016
2017-07-30	57965.462450	2.453 ± 0.167	20.065 ± 1.963	0.0187 ± 0.0016	0.0158 ± 0.0017
2017-10-17	58044.232340	2.202 ± 0.150	28.060 ± 1.955	0.0123 ± 0.0015	0.0183 ± 0.0015
2018-06-28	58298.458450	1.923 ± 0.185	21.125 ± 2.769	0.0142 ± 0.0018	0.0129 ± 0.0019
2018-09-02	58364.407380	2.779 ± 0.182	24.458 ± 1.884	0.0183 ± 0.0018	0.0209 ± 0.0018
2019-06-17	58652.420420	1.973 ± 0.132	25.674 ± 1.917	0.0123 ± 0.0013	0.0154 ± 0.0013
2019-07-14	58679.391810	1.997 ± 0.122	23.489 ± 1.749	0.0136 ± 0.0012	0.0146 ± 0.0012
2019-08-25	58721.425030	2.095 ± 0.115	26.609 ± 1.582	0.0125 ± 0.0012	0.0168 ± 0.0011
2019-09-17	58744.313120	1.820 ± 0.114	26.323 ± 1.801	0.0110 ± 0.0011	0.0145 ± 0.0011
2019-10-21	58778.230810	1.696 ± 0.110	19.862 ± 1.857	0.0130 ± 0.0011	0.0108 ± 0.0011

Table B5: Results for KS1947+300 (after Interstellar Polarization correction) - continued.

Date	JD (2 400 000+)	PD(%)	EVPA (°)	q	u
2019-10-29	58786.194110	1.808 ± 0.115	21.576 ± 1.827	0.0132 ± 0.0011	0.0124 ± 0.0012
2020-06-19	59019.516380	1.969 ± 0.105	30.683 ± 1.526	0.0094 ± 0.0011	0.0173 ± 0.0010
2020-07-01	59031.501810	1.967 ± 0.108	24.980 ± 1.574	0.0126 ± 0.0011	0.0151 ± 0.0011
2020-08-13	59075.304480	1.831 ± 0.113	23.767 ± 1.777	0.0124 ± 0.0011	0.0135 ± 0.0011
2021-06-17	59382.557950	2.057 ± 0.116	24.684 ± 1.618	0.0134 ± 0.0012	0.0156 ± 0.0012
2021-07-17	59412.518580	2.054 ± 0.116	25.935 ± 1.617	0.0127 ± 0.0012	0.0162 ± 0.0011
2021-08-16	59443.351070	2.313 ± 0.119	24.617 ± 1.472	0.0151 ± 0.0012	0.0175 ± 0.0012
2021-08-25	59452.289530	2.224 ± 0.120	24.391 ± 1.552	0.0146 ± 0.0012	0.0167 ± 0.0012
2021-10-07	59495.223080	2.115 ± 0.124	29.390 ± 1.678	0.0110 ± 0.0013	0.0181 ± 0.0012
2022-06-25	59755.533040	2.016 ± 0.117	26.943 ± 1.671	0.0119 ± 0.0012	0.0163 ± 0.0012
2022-06-30	59761.441390	2.123 ± 0.115	29.483 ± 1.557	0.0109 ± 0.0012	0.0182 ± 0.0011
2022-07-15	59776.357410	2.197 ± 0.123	25.971 ± 1.605	0.0135 ± 0.0013	0.0173 ± 0.0012
2023-06-25	60120.509410	1.980 ± 0.116	24.286 ± 1.680	0.0131 ± 0.0012	0.0149 ± 0.0012
2023-07-27	60153.373380	2.171 ± 0.120	31.163 ± 1.581	0.0101 ± 0.0013	0.0192 ± 0.0012
2023-08-24	60181.437870	2.140 ± 0.117	29.867 ± 1.572	0.0108 ± 0.0012	0.0185 ± 0.0011
2023-09-25	60213.284070	1.777 ± 0.125	29.871 ± 2.016	0.0089 ± 0.0013	0.0154 ± 0.0012

Table B6: Results for EXO2030+375 (after Interstellar Polarization correction).

Date	JD (2 400 000+)	PD(%)	EVPA (°)	q	u
2013-10-06	56572.394490	10.574 ± 0.548	44.859 ± 1.485	0.0005 ± 0.0080	0.1057 ± 0.0055
2013-10-21	56587.405930	10.636 ± 0.624	44.458 ± 1.683	0.0020 ± 0.0085	0.1063 ± 0.0062
2013-10-29	56595.373090	12.323 ± 0.537	45.155 ± 1.247	-0.0007 ± 0.0084	0.1232 ± 0.0054
2014-05-31	56808.589910	6.133 ± 1.031	35.478 ± 4.911	0.0200 ± 0.0109	0.0580 ± 0.0102
2014-08-02	56871.526220	9.964 ± 0.637	40.391 ± 1.839	0.0160 ± 0.0083	0.0984 ± 0.0063
2014-08-17	56886.557810	10.279 ± 0.563	48.686 ± 1.572	-0.0132 ± 0.0080	0.1019 ± 0.0056
2014-10-16	56947.339750	11.742 ± 0.637	48.404 ± 1.558	-0.0139 ± 0.0089	0.1166 ± 0.0063
2014-10-20	56951.401740	10.864 ± 0.485	44.243 ± 1.278	0.0029 ± 0.0077	0.1086 ± 0.0048
2014-10-21	56952.236270	11.488 ± 0.513	49.045 ± 1.279	-0.0162 ± 0.0080	0.1137 ± 0.0050
2014-10-23	56954.375810	11.470 ± 0.472	42.085 ± 1.179	0.0117 ± 0.0076	0.1141 ± 0.0047
2015-06-11	57184.511680	13.185 ± 0.576	44.556 ± 1.251	0.0020 ± 0.0091	0.1318 ± 0.0058
2015-07-06	57209.576360	11.512 ± 0.680	42.023 ± 1.696	0.0119 ± 0.0091	0.1145 ± 0.0068
2015-08-06	57240.535050	14.985 ± 0.688	47.026 ± 1.315	-0.0106 ± 0.0099	0.1495 ± 0.0069
2016-05-11	57519.567420	9.806 ± 0.473	44.696 ± 1.383	0.0010 ± 0.0074	0.0981 ± 0.0047
2016-06-15	57555.434230	10.791 ± 0.528	34.361 ± 1.402	0.0392 ± 0.0074	0.1006 ± 0.0049
2016-10-03	57665.268070	10.807 ± 0.398	42.877 ± 1.056	0.0080 ± 0.0072	0.1078 ± 0.0040
2016-11-02	57695.254310	9.860 ± 0.378	45.389 ± 1.099	-0.0013 ± 0.0068	0.0986 ± 0.0038
2017-06-24	57929.456330	9.715 ± 0.438	38.507 ± 1.291	0.0218 ± 0.0069	0.0947 ± 0.0042
2017-07-10	57945.433100	12.042 ± 0.623	44.664 ± 1.484	0.0014 ± 0.0089	0.1204 ± 0.0062
2017-07-30	57965.480190	11.987 ± 0.427	48.103 ± 1.021	-0.0130 ± 0.0076	0.1192 ± 0.0042
2017-10-19	58046.249110	11.149 ± 0.375	44.658 ± 0.963	0.0013 ± 0.0071	0.1115 ± 0.0037
2018-09-01	58363.429900	9.160 ± 0.405	35.873 ± 1.266	0.0287 ± 0.0063	0.0870 ± 0.0037
2018-11-03	58426.239230	12.053 ± 0.373	47.377 ± 0.887	-0.0100 ± 0.0073	0.1201 ± 0.0037
2019-08-25	58721.460310	10.303 ± 0.365	40.957 ± 1.016	0.0145 ± 0.0067	0.1020 ± 0.0036
2020-08-14	59076.308500	10.308 ± 0.410	48.065 ± 1.139	-0.0110 ± 0.0070	0.1025 ± 0.0040
2021-06-18	59383.539630	9.169 ± 0.387	44.512 ± 1.211	0.0016 ± 0.0067	0.0917 ± 0.0039
2021-07-27	59423.383710	9.101 ± 0.453	43.705 ± 1.427	0.0041 ± 0.0071	0.0909 ± 0.0045
2021-08-15	59442.301000	9.615 ± 0.399	49.312 ± 1.188	-0.0144 ± 0.0068	0.0951 ± 0.0039
2021-08-16	59443.295720	9.593 ± 0.451	47.074 ± 1.347	-0.0069 ± 0.0071	0.0957 ± 0.0045
2021-08-17	59444.336780	8.028 ± 0.515	45.902 ± 1.842	-0.0025 ± 0.0072	0.0802 ± 0.0051
2021-08-18	59445.299650	3.435 ± 0.492	47.094 ± 4.165	-0.0025 ± 0.0063	0.0343 ± 0.0049
2021-08-24	59451.378430	8.092 ± 0.511	44.886 ± 1.813	0.0003 ± 0.0071	0.0809 ± 0.0051
2021-09-13	59471.475170	8.141 ± 0.456	42.459 ± 1.609	0.0072 ± 0.0070	0.0811 ± 0.0045
2021-10-07	59495.302630	11.391 ± 0.399	49.724 ± 1.004	-0.0187 ± 0.0073	0.1124 ± 0.0039
2021-10-08	59496.253660	8.833 ± 0.410	44.189 ± 1.330	0.0025 ± 0.0068	0.0883 ± 0.0041
2022-06-01	59732.432420	9.830 ± 0.476	55.108 ± 1.388	-0.0340 ± 0.0071	0.0922 ± 0.0043
2022-06-09	59739.502520	8.292 ± 0.379	47.646 ± 1.309	-0.0076 ± 0.0065	0.0826 ± 0.0038
2023-06-24	60119.557110	11.327 ± 0.341	44.565 ± 0.863	0.0017 ± 0.0070	0.1133 ± 0.0034
2023-08-24	60181.391170	7.434 ± 0.528	51.811 ± 2.043	-0.0175 ± 0.0063	0.0722 ± 0.0052

Table B7: Results for 4U0115+63 (after Interstellar Polarization correction).

Date	JD (2 400 000+)	PD(%)	EVPA (°)	q	u
2013-10-10	56576.499700	2.117 ± 0.280	12.223 ± 3.836	0.0193 ± 0.0028	0.0088 ± 0.0027
2013-10-26	56592.465160	1.262 ± 0.248	24.315 ± 5.771	0.0083 ± 0.0024	0.0095 ± 0.0025
2013-11-26	56623.361810	2.760 ± 0.229	30.287 ± 2.393	0.0136 ± 0.0022	0.0240 ± 0.0023
2014-07-16	56854.592320	1.260 ± 0.264	37.480 ± 6.188	0.0033 ± 0.0025	0.0122 ± 0.0027
2014-08-03	56872.540190	0.277 ± 0.296	-29.447 ± 61.442	0.0014 ± 0.0029	-0.0024 ± 0.0030
2014-08-16	56885.512070	0.587 ± 0.293	21.015 ± 17.207	0.0044 ± 0.0029	0.0039 ± 0.0030
2015-08-30	57264.512470	1.137 ± 0.296	39.834 ± 7.808	0.0020 ± 0.0028	0.0112 ± 0.0030
2015-11-19	57346.353250	1.147 ± 0.235	35.719 ± 6.036	0.0037 ± 0.0022	0.0109 ± 0.0024
2016-06-16	57555.547060	1.308 ± 0.214	34.425 ± 4.776	0.0047 ± 0.0020	0.0122 ± 0.0022
2016-09-10	57641.537170	1.348 ± 0.206	32.887 ± 4.449	0.0055 ± 0.0020	0.0123 ± 0.0021
2016-10-03	57665.438480	1.092 ± 0.204	28.140 ± 5.496	0.0061 ± 0.0020	0.0091 ± 0.0021
2017-06-25	57929.563280	1.205 ± 0.214	50.646 ± 5.195	-0.0024 ± 0.0019	0.0118 ± 0.0022
2017-07-22	57957.476750	0.602 ± 0.207	31.292 ± 10.738	0.0028 ± 0.0020	0.0053 ± 0.0021
2017-07-31	57966.495730	1.261 ± 0.204	30.407 ± 4.725	0.0062 ± 0.0019	0.0110 ± 0.0021
2017-08-05	57970.560680	0.797 ± 0.204	10.821 ± 7.678	0.0074 ± 0.0020	0.0029 ± 0.0020
2017-08-20	57985.615250	0.800 ± 0.223	0.430 ± 8.426	0.0080 ± 0.0022	0.0001 ± 0.0022
2017-08-21	57986.539090	0.891 ± 0.212	9.390 ± 7.088	0.0084 ± 0.0021	0.0029 ± 0.0021
2017-08-29	57994.595020	1.270 ± 0.206	18.160 ± 4.721	0.0102 ± 0.0021	0.0075 ± 0.0021
2017-09-18	58015.483720	0.620 ± 0.227	-5.582 ± 11.548	0.0061 ± 0.0023	-0.0012 ± 0.0022
2017-09-24	58020.547200	1.062 ± 0.220	16.351 ± 6.114	0.0089 ± 0.0022	0.0057 ± 0.0022
2017-10-17	58043.523370	1.620 ± 0.237	37.836 ± 4.253	0.0040 ± 0.0022	0.0157 ± 0.0024
2018-06-30	58299.575500	1.446 ± 0.285	60.118 ± 5.811	-0.0073 ± 0.0027	0.0125 ± 0.0029
2018-07-09	58308.543110	1.480 ± 0.233	61.335 ± 4.589	-0.0080 ± 0.0021	0.0125 ± 0.0024
2018-09-02	58363.586450	0.867 ± 0.222	36.305 ± 7.689	0.0026 ± 0.0021	0.0083 ± 0.0022
2018-09-25	58386.506880	0.857 ± 0.230	26.652 ± 8.106	0.0051 ± 0.0022	0.0069 ± 0.0023
2018-11-02	58425.351120	0.894 ± 0.217	34.099 ± 7.239	0.0033 ± 0.0021	0.0083 ± 0.0022
2019-08-24	58720.485150	1.910 ± 0.212	29.791 ± 3.212	0.0097 ± 0.0021	0.0165 ± 0.0022
2019-09-17	58743.555710	1.931 ± 0.214	26.150 ± 3.202	0.0118 ± 0.0021	0.0153 ± 0.0022
2019-10-12	58769.422840	1.701 ± 0.222	23.691 ± 3.786	0.0115 ± 0.0022	0.0125 ± 0.0023
2019-10-14	58771.482260	1.366 ± 0.241	32.919 ± 5.169	0.0056 ± 0.0023	0.0125 ± 0.0024
2020-07-01	59031.568260	0.967 ± 0.228	52.672 ± 7.014	-0.0026 ± 0.0021	0.0093 ± 0.0023
2020-07-04	59034.557190	0.794 ± 0.230	34.059 ± 8.817	0.0030 ± 0.0022	0.0074 ± 0.0023
2020-07-06	59036.570860	1.177 ± 0.251	26.366 ± 6.306	0.0071 ± 0.0024	0.0094 ± 0.0026
2020-08-29	59090.550170	0.519 ± 0.222	19.804 ± 13.995	0.0040 ± 0.0022	0.0033 ± 0.0022
2020-08-29	59090.556930	0.527 ± 0.235	23.808 ± 14.794	0.0036 ± 0.0023	0.0039 ± 0.0024
2020-09-03	59095.549790	1.867 ± 0.238	27.661 ± 3.698	0.0106 ± 0.0023	0.0154 ± 0.0024
2020-09-06	59098.502950	0.950 ± 0.238	26.565 ± 7.492	0.0057 ± 0.0023	0.0076 ± 0.0024
2020-09-25	59117.570840	1.355 ± 0.216	20.076 ± 4.652	0.0104 ± 0.0022	0.0087 ± 0.0022
2021-06-19	59384.558510	1.399 ± 0.233	46.249 ± 4.852	-0.0006 ± 0.0021	0.0140 ± 0.0023
2021-08-16	59442.506320	1.755 ± 0.217	29.627 ± 3.582	0.0090 ± 0.0021	0.0151 ± 0.0022
2021-09-23	59480.588740	0.548 ± 0.293	46.308 ± 18.962	-0.0003 ± 0.0028	0.0055 ± 0.0029
2021-09-27	59484.511070	0.847 ± 0.224	28.596 ± 7.965	0.0046 ± 0.0022	0.0071 ± 0.0023
2021-10-07	59495.416280	2.035 ± 0.226	33.885 ± 3.201	0.0077 ± 0.0021	0.0188 ± 0.0023
2023-06-26	60121.562450	1.538 ± 0.218	33.318 ± 4.120	0.0061 ± 0.0021	0.0141 ± 0.0022
2023-07-28	60153.562060	0.747 ± 0.213	19.593 ± 8.634	0.0058 ± 0.0021	0.0047 ± 0.0021
2023-08-25	60181.543830	0.878 ± 0.217	40.907 ± 7.402	0.0013 ± 0.0021	0.0087 ± 0.0022
2023-09-25	60213.410710	1.111 ± 0.221	32.594 ± 5.858	0.0047 ± 0.0021	0.0101 ± 0.0022

Bibliography

Baade, D. (1999). Non-radial pulsations of ba supergiants and be stars. In *International Astronomical Union Colloquium*, volume 169, pages 312–319. Cambridge University Press.

Bahramian, A. and Degenaar, N. (2022). Low-mass x-ray binaries. *arXiv preprint arXiv:2206.10053*.

Blinov, D., Kiehlmann, S., Pavlidou, V., Panopoulou, G., Skalidis, R., Angelakis, E., Casadio, C., Einoder, E., Hovatta, T., Kokolakis, K., et al. (2021). Robopol: Agn polarimetric monitoring data. *Monthly Notices of the Royal Astronomical Society*, 501(3):3715–3726.

Borozdin, K., Gilfanov, M., BRINKMAN, A., HEISE, J., IN'T ZAND, J. M., and JAGER, R. (1990). The new x-ray transient source ks 1947+ 300 in cygnus constellation. *Pis ma v Astronomičeskij žurnal*, 16(9):804–807.

Carciofi, A. C. and Bjorkman, J. E. (2006). Non-lte monte carlo radiative transfer. i. the thermal properties of keplerian disks around classical be stars. *The Astrophysical Journal*, 639(2):1081.

Carciofi, A. C., Okazaki, A., Le Bouquin, J.-B., Štefl, S., Rivinius, T., Baade, D., Bjorkman, J., and Hummel, C. (2009). Cyclic variability of the circumstellar disk of the be star ζ tauri-ii. testing the 2d global disk oscillation model. *Astronomy & Astrophysics*, 504(3):915–927.

Cominsky, L., Clark, G., Li, F., Mayer, W., and Rappaport, S. (1978). Discovery of 3· 6-s x-ray pulsations from 4u0115+ 63. *Nature*, 273(5661):367–369.

Giacconi, R., Murray, S., Gursky, H., Kellogg, E., Schreier, E., and Tananbaum, H. (1972). The uhuru catalog of x-ray sources. *Astrophysical Journal, Vol. 178, p. 281-308*, 178:281–308.

Halonen, R., Mackay, F., and Jones, C. (2013). Computing the continuum polarization from thomson scattering in gaseous circumstellar disks. *The Astrophysical Journal Supplement Series*, 204(1):11.

Halonen, R. J. and Jones, C. E. (2013). On the intrinsic continuum linear polarization of classical be stars: The effects of metallicity and one-armed density perturbations. *The Astrophysical Journal Supplement Series*, 208(1):3.

Hanuschik, R., Hummel, W., Dietle, O., and Sutorius, E. (1995). V/r variability and global oscillations in be star disks. *Astronomy and Astrophysics*, 300:163.

Haubois, X., Mota, B. C., Carciofi, A. C., Draper, Z. H., Wisniewski, J. P., Bednarski, D., and Rivinius, T. (2014). Dynamical evolution of viscous disks around be stars. ii. polarimetry. *The Astrophysical Journal*, 785(1):12.

Johns, M., Koski, A., Canizares, C., McClintock, J., Rappaport, S., Clark, G., Cominsky, L., and Li, F. (1978). 4u 0115+ 63. *International Astronomical Union Circular*, 3171:1.

King, O., Blinov, D., Ramaprakash, A., Myserlis, I., Angelakis, E., Baloković, M., Feiler, R., Fuhrmann, L., Hovatta, T., Khodade, P., et al. (2014). The robopol pipeline and control system. *Monthly Notices of the Royal Astronomical Society*, 442(2):1706–1717.

Martin, R. G., Nixon, C., Armitage, P. J., Lubow, S. H., and Price, D. J. (2014). Giant outbursts in be/x-ray binaries. *The Astrophysical Journal Letters*, 790(2):L34.

Martin, R. G., Pringle, J., Tout, C. A., and Lubow, S. H. (2011). Tidal warping and precession of be star decretion discs. *Monthly Notices of the Royal Astronomical Society*, 416(4):2827–2839.

Moritani, Y., Nogami, D., Okazaki, A. T., Imada, A., Kambe, E., Honda, S., Hashimoto, O., Mizoguchi, S., Kanda, Y., Sadakane, K., et al. (2013). Precessing warped be disk triggering the giant outbursts in 2009 and 2011 in a 0535+ 262/v725 tau. *Publications of the Astronomical Society of Japan*, 65(4):83.

Negueruela, I. (1998). On the nature of be/x-ray binaries. *Astronomy Astrophysics*.

Negueruela, I., Israel, G. L., Marco, A., Norton, A. J., and Speziali, R. (2003). The be/x-ray transient ks 1947+ 300. *Astronomy & Astrophysics*, 397(2):739–745.

Negueruela, I. and Okazaki, A. T. (2001). The be/x-ray transient 4u 0115+ 63/v635 cassiopeiae-i. a consistent model. *Astronomy & Astrophysics*, 369(1):108–116.

Negueruela, I., Smith, D. M., Reig, P., Chaty, S., and Torrejon, J. M. (2005). Supergiant fast x-ray transients: a new class of high mass x-ray binaries unveiled by integral. *arXiv preprint astro-ph/0511088*.

Norton, A., Chakrabarty, D., Coe, M., Everall, C., Finger, M., Prince, T., Roche, P., Stollberg, M., and Wilson, R. (1994). Multiwavelength observations of the be star/x-ray binary exo2030+ 375 during outburst. *Monthly Notices of the Royal Astronomical Society*, 271(4):981–992.

Okazaki, A. (1997). On the confinement of one-armed oscillations in discs of be stars. *Astronomy and Astrophysics, v. 318, p. 548-560*, 318:548–560.

Okazaki, A. and Negueruela, I. (2001). A natural explanation for periodic x-ray outbursts in be/x-ray binaries. *Astronomy & Astrophysics*, 377(1):161–174.

Okazaki, A. T. (1991). Long-term v/r variations of be stars due to global one-armed oscillations of equatorial disks. *Publications of the Astronomical Society of Japan*, 43:75–94.

Okazaki, A. T., Hayasaki, K., and Moritani, Y. (2013). Origin of two types of x-ray outbursts in be/x-ray binaries. i. accretion scenarios. *Publications of the Astronomical Society of Japan*, 65(2):41.

Orellana, M. and Romero, G. E. (2005). Gamma-ray emission from be/x-ray binaries. *Astrophysics and Space Science*, 297:167–178.

Panopoulou, G., Tassis, K., Blinov, D., Pavlidou, V., King, O., Paleologou, E., Ramaprakash, A., Angelakis, E., Baloković, M., Das, H., et al. (2015). Optical polarization map of the polaris flare with robopol. *Monthly Notices of the Royal Astronomical Society*, 452(1):715–726.

Parmar, A., White, N., Stella, L., Izzo, C., and Ferri, P. (1989). The transient 42 second x-ray pulsar exo 2030+ 375. i-the discovery and the luminosity dependence of the pulse period variations. *Astrophysical Journal, Part 1 (ISSN 0004-637X), vol. 338, March 1, 1989, p. 359-372.*, 338:359–372.

Poeckert, R., Bastien, P., and Landstreet, J. (1979). Intrinsic polarization of be stars. *Astronomical Journal, vol. 84, June 1979, p. 812-830. Research supported by the National Research Council of Canada.*, 84:812–830.

Porter, J. M. and Rivinius, T. (2003). Classical be stars. *Publications of the Astronomical Society of the Pacific*, 115(812):1153.

Ramaprakash, A., Rajarshi, C., Das, H., Khodade, P., Modi, D., Panopoulou, G., Maharana, S., Blinov, D., Angelakis, E., Casadio, C., et al. (2019). Robopol: a four-channel optical imaging polarimeter. *Monthly Notices of the Royal Astronomical Society*, 485(2):2355–2366.

Rappaport, S., Clark, G., Cominsky, L., Joss, P., and Li, F. (1978). Orbital elements of 4u 0115+ 63 and the nature of the hard x-ray transients. *Astrophysical Journal, Part 2-Letters to the Editor, vol. 224, Aug. 15, 1978, p. L1-L4.*, 224:L1–L4.

Reig, P. (2011). Be/x-ray binaries. *Astrophysics and Space Science*, 332(1):1–29.

Reig, P., Blinov, D., Papadakis, I., Kylafis, N., and Tassis, K. (2014). The high optical polarization in the be/x-ray binary exo 2030+ 375. *Monthly Notices of the Royal Astronomical Society*, 445(4):4235–4240.

Reig, P., Fabregat, J., and Coe, M. (1997). A new correlation for be/x-ray binaries: the orbital period-halpha equivalent width diagram. *Astronomy and Astrophysics*, 322:193–196.

Reig, P., Nersesian, A., Zezas, A., Gkouvelis, L., and Coe, M. J. (2016). Long-term optical variability of high-mass X-ray binaries. II. Spectroscopy. , 590:A122.

Reig, P. and Roche, P. (1999). Discovery of two new persistent be/x-ray pulsar systems. *Monthly Notices of the Royal Astronomical Society*, 306(1):100–106.

Reig, P., Tzouvanou, A., Blinov, D., and Pantoulas, V. (2023). Long-term optical variability of the be/x-ray binary gro j2058+ 42. *Astronomy & Astrophysics*, 671:A48.

Revnivtsev, M. and Mereghetti, S. (2016). Magnetic fields of neutron stars in x-ray binaries. *The Strongest Magnetic Fields in the Universe*, pages 299–320.

Rivinius, T., Carciofi, A. C., and Martayan, C. (2013). Classical be stars. *The Astronomy and Astrophysics Review*, 21(1):1–86.

Roche, P., Larionov, V., Tarasov, A., Fabregat, J., Clark, J., Coe, M., Kalv, P., Larionova, L., Negueruela, I., Norton, A., et al. (1997). Observations of the recent disc loss in x persei: photometry and polarimetry. *Astronomy and Astrophysics, v. 322, p. 139-146*, 322:139–146.

Slettebak, A. (1982). Spectral types and rotational velocities of the brighter be stars and af type shell stars. *Astrophysical Journal Supplement Series, vol. 50, Sept. 1982, p. 55-83.*, 50:55–83.

Steele, I., Negueruela, I., and Clark, J. (1999). A representative sample of be stars-i. sample selection, spectral classification and rotational velocities. *Astronomy and Astrophysics Supplement Series*, 137(1):147–156.

Tauris, T. and Van Den Heuvel, E. (2006). Formation and evolution of compact stellar x-ray sources. *Cambridge Astrophysics Series*, 39:623.

Telting, J., Heemskerk, M., Henrichs, H., and Savonije, G. (1994). Observational evidence for a prograde one-armed density structure in the equatorial disc of a be star. *Astronomy and Astrophysics*, 288:558–560.

Wilson, C. A., Finger, M. H., and Camero-Arranz, A. (2008). Outbursts large and small from exo 2030+ 375. *The Astrophysical Journal*, 678(2):1263.

Wisniewski, J. P., Draper, Z. H., Bjorkman, K. S., Meade, M. R., Bjorkman, J. E., and Kowalski, A. F. (2010). Disk-loss and disk-renewal phases in classical be stars. i. analysis of long-term spectropolarimetric data. *The Astrophysical Journal*, 709(2):1306.

Wood, K., Bjorkman, J., Whitney, B., and Code, A. (1996). The effect of multiple scattering on the polarization from axisymmetric circumstellar envelopes. ii. thomson scattering in the presence of absorptive opacity sources. *Astrophysical Journal v. 461, p. 847*, 461:847.

Yudin, R. (2001). Statistical analysis of intrinsic polarization, ir excess and projected rotational velocity distributions of classical be stars. *Astronomy & Astrophysics*, 368(3):912–931.

URL References

1. RoboPol: https://robopol.physics.uoc.gr/
2. Non-Radial-Pulsations: http://www.physics.usyd.edu.au/~bedding/animations/visual.html
3. RXTE/ASM: https://heasarc.gsfc.nasa.gov/docs/xte/learning_center/asm.html
4. BATSE: https://heasarc.gsfc.nasa.gov/docs/cgro/cgro/batse.html
5. EXOSAT: https://www.cosmos.esa.int/web/exosat
6. Swift/XRT https://swift.gsfc.nasa.gov/about_swift/xrt_desc.html
7. KS1947+300: https://simbad.u-strasbg.fr/simbad/sim-id?Ident=KS+1947%2B300&NbIdent=1&Radius=2&Radius.unit=arcmin&submit=submit+id
8. KS1947+300 info: http://astro.uni-tuebingen.de/~xrbcat/HMXBHTMLfile/KS%201947+300.html
9. EXO2030+375: https://simbad.u-strasbg.fr/simbad/sim-id?Ident=EXO+2030%2B375
10. EXO2030+375 info: http://astro.uni-tuebingen.de/~xrbcat/HMXBHTMLfile/EXO%202030+375.html
11. 4U0115+63: https://simbad.u-strasbg.fr/simbad/sim-id?Ident=4U+0115%2B63
12. 4U0115+63 info: http://astro.uni-tuebingen.de/~xrbcat/HMXBHTMLfile/4U%200115+63.html